2
3
4
5
6
7
8
9
10
11

An assessment of natural methane fluxes simulated by the CLASS-CTEM model

Vivek K. Arora[1], Joe R. Melton[2], and David Plummer[1].

[1]Canadian Centre for Climate Modelling and Analysis, Environment and Climate Change Canada,
University of Victoria, Victoria, B.C., V8W 2Y2, Canada

[2]Climate Research Division, Environment and Climate Change Canada,
Victoria, B.C., Canada

Abstract

Natural methane emissions from wetlands and fire, and soil uptake of methane, simulated using the Canadian Land Surface Scheme and Canadian Terrestrial Ecosystem (CLASS-CTEM) modelling framework, over the historical 1850-2008 period, are assessed by using a one box model of atmospheric methane burden. This one box model also requires anthropogenic emissions and the methane sink in the atmosphere to simulate the historical evolution of global methane burden. For this purpose, global anthropogenic methane emissions for the period 1850-2008 were reconstructed based on the harmonized representative concentration pathway (RCP) and Emission Database for Global Atmospheric Research (EDGAR) data sets. The methane sink in the atmosphere is represented using bias-corrected methane lifetimes from the Canadian Middle Atmosphere Model (CMAM). The resulting evolution of atmospheric methane concentration over the historical period compares reasonably well with observation-based estimates (correlation=0.99, root mean square error = 35 ppb). The modelled natural emissions are also assessed using an inverse procedure where the methane lifetimes required to reproduce the observed year-to-year increase in atmospheric methane burden are calculated based upon the global anthropogenic and modelled natural emissions that we have used here. These calculated methane lifetimes over the historical period fall within the uncertainty range of observation-based estimates. The present-day (2000-2008) values of modelled methane emissions from wetlands (169 Tg CH_4/yr) and fire (27 Tg CH_4/yr), methane uptake by soil (29 Tg CH_4/yr), and the budget terms associated with overall anthropogenic and natural emissions are consistent with estimates reported in a recent global methane budget that is based on top-down approaches constrained by observed atmospheric methane burden. The modelled wetland emissions increase over the historical period in response to both increase in precipitation and increase in atmospheric CO_2 concentration. This increase in wetland emissions over the historical period yields evolution of the atmospheric methane concentration that compares better with observation-based values than the case when wetland emissions are held constant over the historical period.

1. Introduction

Earth system models (ESMs) represent physical climate system processes and their interactions with biogeochemical processes focusing primarily on the carbon cycle in the context of carbon dioxide (CO_2). These models are able to project how the atmospheric concentration of carbon dioxide ($[CO_2]$) will change in response to changes in anthropogenic CO_2 emissions or alternatively diagnose anthropogenic CO_2 emissions required to achieve a specific CO_2 concentration pathway (Jones et al., 2013). This capability is achieved by modelling $[CO_2]$ as a prognostic variable which itself requires modelling of the surface-atmosphere exchange of CO_2 and hence the need for land and oceanic carbon cycle components in ESMs (Arora et al. 2013; Friedlingstein et al. 2006; Friedlingstein et al. 2014). While most ESMs include the capability of modelling $[CO_2]$ as a prognostic variable there are only a handful of ESMs which are beginning to treat the atmospheric concentration of methane, ($[CH_4]$), as a fully prognostic variable (Collins et al., 2011; Shindell et al., 2013).

The $[CH_4]$ has increased from 700 ± 25 ppb in 1750 to 1795 ± 18 ppb in 2010 (Prather et al., 2012). The $[CO_2]$ has increased globally from 278 (276–280) ppm in 1750 to 390.5 (390.3–390.7) ppm in 2011. The greater global warming potential of CH_4 compared to CO_2 (84 and 28 for 20-years and 100-year time scales, respectively), has made methane the second most radiatively important greenhouse gas (GHG) after carbon dioxide CO_2 (Myhre et al., 2013). The CO_2 radiative forcing for the period 1750-2011 is 1.82 W/m^2 (associated with ~112 ppm increase), while the radiative forcing for CH_4 over the same period is 0.48 W/m^2 (associated with ~1081 ppb = 1.08 ppm increase) (Myhre et al., 2013). Since methane is a short-lived GHG with an atmospheric lifetime of around 9 years (compared to CO_2 which has an atmospheric lifetime of around 100-200 years), mitigation of anthropogenic CH_4 emissions

85   can lead to a decrease in its atmospheric concentration within a timeframe of 10-20 years. As

86   a result methane is considered a short-lived climate forcer (SLCF) and therefore reduction in

87   its anthropogenic emissions offers an attractive and potentially viable target for short-term

88   climate change mitigation policies (Shindell et al., 2012). To be able to address climate

89   benefits of reduction in anthropogenic CH_4 emissions within the framework of

90   comprehensive ESMs, however, it is necessary to model [CH_4] as a prognostic variable in

91   these models.

92

93   Treatment of [CH_4] as a fully prognostic variable in ESMs is hindered by at least two factors.

94   First, the global CH_4 budget is not as well understood as for CO_2. Our lack of ability to close

95   the present-day global CH_4 budget is illustrated in Saunois et al. (2016) who present a recent

96   synthesis of several studies and summarize the present-day global CH_4 budget. Saunois et al.

97   (2016) show a large discrepancy between total CH_4 emissions, from both anthropogenic and

98   natural sources, for the 2003-2012 period as inferred from the top-down atmospheric

99   inversion-based approaches (558 Tg CH_4/yr) and those based on bottom-up modelling and

100   other approaches (736 Tg CH_4/yr). The primary reason for this discrepancy is that there are

101   multiple sources of both natural and anthropogenic CH_4 emissions so the bottom-up

102   approaches that add up all the individual sources inevitably give larger total emissions than

103   top-down approaches that are constrained by the atmospheric CH_4 burden and its loss in the

104   atmosphere. Second, unlike CO_2, CH_4 has a sink in the atmosphere which requires

105   representation of atmospheric chemistry in ESMs to properly account for the removal of CH_4

106   and feedbacks of methane on chemistry. CH_4 is destroyed in the troposphere and stratosphere

107   due to its reaction with OH radicals and chlorine. This is typically very computationally

108   expensive to represent. As an example, the model years per wall clock day simulated by the

109   atmospheric component of the second generation Canadian Earth System Model (CanESM2;

110   Arora et al., 2011) are reduced by a factor of around six when atmospheric chemistry is

111   turned on.

112

113   Despite these two challenges there are ways forward to model [CH_4] as a fully prognostic

114   variable and be able to use comprehensive ESMs to ask questions that the climate modelling

115   community has asked so far in the context of CO_2. For example, how would future [CH_4]

116   change in response to changes in anthropogenic and natural CH_4 emissions, or alternatively

117   what should anthropogenic CH_4 emissions be to achieve a given CH_4 concentration pathway,

118   all while as anthropogenic CO_2 emissions continue to increase? In terms of emissions, since

119   the top-down estimates of CH_4 emissions from natural and anthropogenic sources are better

120   constrained than the bottom-up estimates they are likely to provide more robust estimates for

121   evaluating ESMs and their CH_4 related components. The expensive atmospheric chemistry

122   modules can be replaced with simple first-order representations of chemical losses   or,

123   ignoring the spatial variations in CH_4 concentration, the global average concentration of

124   methane can be simulated with a box model using specified methane life times which are

125   calculated a priori using full 3D chemistry-climate models. Although, of course, using

126   specified CH_4 losses implies that feedbacks of methane on methane loss rates and interactions

127   between atmospheric chemistry and climate can be neglected.

128

129   The CLASS-CTEM modelling framework serves as the land surface component in the family

130   of Canadian ESMs (CanESMs) (Arora et al., 2009, 2011; Arora and Scinocca, 2016)

131   developed by the Department of Environment and Climate Change, Government of Canada,

132   and models the land-atmosphere fluxes of water, energy and CO_2. It consists of the Canadian

133   Land Surface Scheme (CLASS) and the Canadian Terrestrial Ecosystem Model (CTEM). In

134   preparation for modelling [CH_4] as a prognostic variable in future versions of CanESMs we

135 have included several CH_4 related processes in the CLASS-CTEM modelling framework.

136 These include representations of dynamic natural wetlands and their CH_4 emissions, CH_4

137 emissions from fires, and uptake of CH_4 by soils. This paper evaluates the simulated spatial

138 distribution of wetlands as well as the magnitude of CH_4 emissions from wetlands and fires,

139 and CH_4 uptake by soils against their respective present-day observation-based estimates. We

140 also evaluate the simulated time evolution of the global sums of these fluxes for the 1850-

141 2008 period by using a one-box model of atmospheric CH_4 burden. This one-box model

142 requires anthropogenic CH_4 emissions, emissions from other natural sources that aren't

143 modelled in the CLASS-CTEM framework, and a representation of atmospheric sinks. The

144 anthropogenic CH_4 emissions for the period 1850-2008 are obtained by harmonizing the RCP

145 and EDGAR data sets, and natural emissions from sources that aren't modelled are specified.

146 Finally, the atmospheric sink of CH_4 is based on bias-corrected global atmospheric lifetime of

147 CH_4 as computed by the Canadian Middle Atmosphere Model (CMAM). The one-box model

148 of atmospheric CH_4 burden is used to evaluate CLASS-CTEM simulated natural CH_4 fluxes

149 by comparing simulated evolution of global $[CH_4]$ with their observation-based estimates as

150 well as by comparing the CH_4 lifetime required to reproduce the observed evolution of global

151 $[CH_4]$ over the historical period with their observation-based estimates.

152

153 The rest of this paper is organized as follows. A brief description of the CLASS-CTEM

154 modelling framework is presented in Section 2 along with the details of methane related

155 processes that are implemented, the data sets used and the experimental protocol. Results are

156 presented in Section 3 and finally discussion and conclusions are presented in Section 4.

157 **2. Model, data and experimental set up**

158 **2.1 The CLASS-CTEM model and its forcing and evaluation data sets**

159 **2.1.1 The CLASS-CTEM model**

160

161 The CLASS-CTEM modelling framework consists of the Canadian Land Surface Scheme

162 (CLASS) and the Canadian Terrestrial Ecosystem Model (CTEM) which are coupled to each

163 other and which together simulate fluxes of energy, water, CO_2 and now CH_4 at the land-

164 atmosphere boundary. Together, CLASS and CTEM form the land surface component in

165 Canadian Earth System Models - CanESM1 (Arora et al., 2009), CanESM2 (Arora et al.,

166 2011), and CanESM4.2 (Arora and Scinocca, 2016).

167

168 CLASS simulates atmosphere-land fluxes of energy and water and it prognostically

169 calculates the liquid and frozen soil moisture contents, and soil temperature for its soil layers,

170 the liquid and frozen moisture contents and temperature of the single vegetation canopy layer

171 (if present) and the snow water equivalent and temperature of a single snow layer (if present).

172 CLASS is described in detail in Verseghy (1991), Verseghy et al. (1993) and Verseghy

173 (2000). In the version 3.6 of CLASS used here, the thicknesses of the three permeable soil

174 layers are specified as 0.1, 0.25 and 3.75 m, although the model can be configured to use any

175 number of layers with specified thicknesses. The thicknesses of the permeable layers also

176 depend on the depth to the bedrock which is specified on the basis of the global data set of

177 (Zobler, 1986). For example, if the depth to bedrock is only 2 m, then the thicknesses of the

178 permeable soil layers are taken to be 0.1, 0.25 and 1.65 m. The energy and water balance

179 calculations are performed for four plant functional types (PFTs) (needleleaf trees, broadleaf

180 trees, crops and grasses). CLASS operates at a sub-daily time step and a time step of 30

181 minutes is used here.

182

183   CTEM simulates the fluxes of CO_2 at the land-atmosphere boundary and in doing so models

184   vegetation as a dynamic component of the climate system. It models photosynthesis,

185   autotrophic respiratory fluxes from its three living vegetation components (leaves, stem and

186   roots, denoted respectively by L, S and R) and heterotrophic respiratory fluxes from its two

187   dead carbon components (litter and soil carbon, denoted respectively by D and H). The flow

188   of carbon through these five carbon pools is explicitly tracked which allows to calculate the

189   amount of carbon in these pools as prognostic variables. Disturbance through fire and land

190   use change are also modelled. CTEM cannot operate without coupling to CLASS. Its

191   photosynthesis module operates at the same time step as CLASS and requires estimates of net

192   radiation and soil moisture from CLASS. In return, CTEM provides CLASS with

193   dynamically simulated structural attributes of vegetation which are functions of the driving

194   meteorological data. The amount of carbon in the leaves, stem and root components is used to

195   estimate structural attributes of vegetation. The leaf area index (LAI) is calculated from leaf

196   biomass using PFT-dependent specific leaf area (SLA, m^2/Kg C) which determines the area

197   of leaves that can be constructed per unit leaf carbon biomass (Arora and Boer, 2005a);

198   vegetation height is calculated based on stem biomass for tree PFTs and LAI for grass PFTs

199   (Arora and Boer, 2005a); and rooting depth is calculated based on root biomass (Arora and

200   Boer, 2003). Other than photosynthesis, all terrestrial ecosystem processes in CTEM are

201   modelled at a daily time step. CTEM models its terrestrial ecosystem processes for nine PFTs

202   that map directly to the PFTs used by CLASS. Needleleaf trees in CTEM are divided into

203   deciduous and evergreen for which terrestrial ecosystem processes are modelled separately,

204   broadleaf trees are divided into cold and drought deciduous and evergreen types, and crops

205   and grasses are divided into C_3 and C_4 versions based on their photosynthetic pathways. The

206   version 2.0 of the model is explained in detail in Melton and Arora (2016), while version 2.1

207   is used here which amongst other minor changes includes all methane related processes

208   discussed below.

209

210   The methane related processes implemented in CLASS-CTEM build on the model's existing

211   capabilities. Processes are implemented to be able to dynamically model the geographical

212   distribution of wetlands and their methane emissions, methane emissions from fire and

213   methane uptake by upland soils. The fractional coverage of wetlands in a grid cell is based on

214   flat fraction within a grid cell with slope less than 0.2% and grid-averaged soil moisture. The

215   methodology is explained in Appendix A.

216   **2.1.1.1 Wetland methane emissions**

217

218   The dominant controls on methane emissions in nature are considered to be 1) the position of

219   the water table below which methane is produced due to anoxic decomposition of available

220   organic matter and above which methane is oxidized, 2) the soil temperature which

221   determines the rate of decomposition of organic matter, 3) the availability of organic matter

222   itself, and 4) the pathway through which methane is transferred to the atmosphere (through

223   soil via molecular diffusion, through stems of the vascular plants and through ebullition if the

224   water table is above the soil surface). These factors are not completely independent and their

225   relative importance changes as environmental conditions change (Walter and Heimann,

226   2000). The explicit consideration of these factors becomes more important as the spatial

227   scale at which CH_4 emissions are being modelled reduces. For example, Zhu et al. (2014b)

228   show that as the modelling spatial scale reduces from 100 to 5 km, the dominant control on

229   simulated wetland CH_4 emissions switches from soil temperature to water table depth.

230

231   At the current operational resolution of around 2.81° of CanESM (equal to about 310 km at

232   the equator) we expect dominant controls on methane emissions to be soil moisture, soil

233   temperature and the availability of organic matter and this allows us to use the simple

234   approach that we have used here. This approach also allows us to estimate CH_4 emissions

235   from wetlands without the use of wetland specific PFTs since at large spatial scales net

236   primary productivity (NPP) and heterotrophic respiration are governed by climate (Chengjin

237   et al., 2016) . CH_4 emissions are simulated to occur over the wetland fraction of the grid cell.

238   The simulated CH_4 emissions from wetlands are calculated by scaling the heterotrophic

239   respiratory flux (R_h) from model's litter (D) and soil (H) carbon pools which itself depends

240   on soil temperature, soil moisture, and the available organic matter. Heterotrophic respiration

241   from the litter and soil carbon pools takes the following basic form, with the formulation

242   explained in detail in Melton and Arora (2016)

243

$$R_{h,i} = 2.64 \times 10^{-6} \varsigma_i \, C_i \, f_i(Q_{10}) f_i(\Psi) \, , i = D, H$$

244    $$R_h = R_{h,D} + R_{h,H} \tag{1}$$

245

246   where ς_i represents the base respiration rate (kg C (kg C)$^{-1}$ year^{-1}) at 15°C, C_i is the amount

247   of carbon in model's litter or soil carbon pool (kg C m^{-2}), $f_i(Q_{10}) = Q_{10}^{0.1(T_i - 15)}$ is a Q_{10}

248   function that models the effect of temperature, T_i is the temperature of litter or soil carbon

249   pool (°C) and $f_i(\Psi)$ is the function that reduces heterotrophic respiration when soils are too

250   dry and too wet using the soil matric potential (Ψ) (Melton et al., 2015). The constant 2.64

251    $\times 10^{-6}$ converts units from kg C m^{-2} yr^{-1} to mol CO_2 m^{-2} s^{-1}.

252

253   Modelled CH_4 emissions from wetlands, per unit area of a grid cell (mol CH_4 m^{-2} s^{-1}), are

254   calculated as

255

$$E_w = R_h \, f_w \, \alpha_w \, \delta_s \tag{2}$$

257

where f_w is the wetland fraction in a grid cell mentioned above, α_w is the ratio of wetland to upland heterotrophic respiratory flux, and δ_s converts flux from CO_2 to CH_4 units but also takes into account that some of the CH_4 flux is oxidized in the soil column before reaching the atmosphere. A value of 0.45 is used for α_w since heterotrophic CO_2 respiratory flux over lowlands is typically lower than over uplands due to limitation by increased soil moisture including a high water table level. While the $f_i(\Psi)$ function in equation (1) does reduce heterotrophic respiration when soils are wet it does so using only the grid averaged soil moisture content. Wania et al. (2010) use a preferred value of δ_s equal to 0.1 and Zhu et al. (2014a) found δ_s varies between 0.1 and 0.7 with a mean value of 0.23 when calibrating their model against data from 19 sites. A value of 0.135 is used for δ_s in this study. The product $\alpha_w \, \delta_s$ thus equals 0.061 which implies that for each mol CO_2 m^{-2} s^{-1} of heterotrophic respiratory flux 0.061 mol CH_4 m^{-2} s^{-1} is generated over unit area that is deemed wetland. At large spatial scales CH_4 and CO_2 heterotrophic respiratory fluxes are expected to be highly correlated since to the first order they are both governed by temperature and the amount of organic matter available for decomposition (Dalva et al., 2001; Zhu et al., 2014a). In addition, as the spatial scale increases it is possible to ignore the effect of water table depth as Zhu et al. (2014b) illustrate.

2.1.1.2 Fire methane emissions

Fire in CLASS-CTEM is modelled using an intermediate complexity scheme, which represents both natural and human-caused fires, and accounts for all elements of the fire

279 triangle: fuel load, combustibility of fuel, and availability of ignition sources. The fire module

280 accounts for both natural fires caused by lightning and anthropogenic fires which are the

281 result of ignitions caused by humans expressed as a function of population density. Increasing

282 population density increases human-caused fire ignitions but also increases suppression of

283 fire. The suppression of fire represents fire-fighting efforts, landscape fragmentation and

284 other processes which leads to a reduction in area burned and is also modelled as a function

285 of population density. The original fire parametrization is described in Arora and Boer

286 (2005b) which has since been adapted and used in several other DGVMs (Kloster et al.,

287 2010; Li et al., 2012; Migliavacca et al., 2013). The fire module in CTEM v. 2.1 incorporates

288 changes suggested in these studies as well as several new improvements which are

289 summarized in detail in Melton and Arora (2016). The approach has been evaluated at the

290 global scale in Arora and Melton (2018) who assess how reduction in global wildfire

291 emissions since 1930s leads to an enhanced land carbon sink. The two primary outputs from

292 the fire module are fraction of area burned per grid cell and dry organic biomass burned per

293 unit area ($gC\ m^{-2}$). The dry organic matter burned is then multiplied by corresponding

294 emissions factors to obtained emissions (g species m^{-2}) for several species of trace gases and

295 aerosols including methane (CO_2, CO, CH_4, H_2, NHMC, NO_x, N_2O, total particulate matter,

296 particulate matter less than 2.5 μm in diameter, and black and organic carbon). These

297 emissions factors are based on an updated set by Andreae and Merlet (2001) listed in Tables

298 3 and 4 of Li et al. (2012).

299 **2.1.1.3 Soil uptake of methane**

300

301 The methane uptake over soil occurs over the unsaturated (upland) fraction of a grid cell that

302 is not deemed wetland. The parameterization is based on an exact solution of the one-

303 dimensional diffusion-reaction equation in the near-surface (top) soil layer and described in

304   detail in Curry (2007). Briefly, the methane uptake by soil is a function of diffusion of

305   methane into soil (which depends on atmospheric methane concentration) and its subsequent

306   oxidation by microbes. The diffusion of methane into the soil depends primarily on air filled

307   porosity of the soil and increases as the pore volume filled by liquid and frozen moisture

308   decreases. The oxidation of methane by microbes is a function of both soil moisture and

309   temperature. Oxidation preferably occurs when soils are neither too dry (when microbial

310   activity is limited by low soil moisture) and nor too wet (when microbes are deprived of

311   oxygen). Warmer temperatures favour oxidation of methane in soil and oxidation increases

312   by about 4 times as soil temperature increases from 0 °C to 27.5 °C. Finally, the inhibition of

313   methane uptake in cultivated soils is accounted for by a linear factor that reduces oxidation as

314   crop fraction in a grid cell increases.

315   **2.1.2 Forcing data for the CLASS-CTEM model**

316

317   The CLASS-CTEM model is driven with meteorological data and atmospheric CO_2 and CH_4

318   concentrations. The model also requires geophysical fields for the fractional coverage of nine

319   CTEM PFTs, soil texture and depth to bedrock. The meteorological data are based on version

320   7 of the Climate Research Unit – National Centre for Environmental Prediction (CRU-NCEP)

321   reanalysis dataset (Viovy, 2012). The meteorological variables (surface temperature,

322   pressure, precipitation, wind, specific humidity, and incident short-wave and long-wave

323   radiation fluxes) are available at a spatial resolution of 0.5° × 0.5° and at a six hourly time

324   interval for the period 1901-2015. These data are regridded to a spatial resolution of 2.81°

325   and temporally to a half-hour time step to drive the CLASS-CTEM model. Temperature,

326   pressure, wind, specific humidity, and long-wave radiation are linearly interpolated in time

327   while short-wave radiation is assumed to change with the solar zenith angle with maximum

328   radiation occurring at solar noon. Following Arora (1997) the six-hourly precipitation amount

329   (P, mm/6-hour) is used to estimate the number of wet half-hours in a given six-hour period

330   and the six- hourly precipitation amount is randomly distributed over these wet half hours.

331   Figure B1 in Appendix B shows the annual land-averaged temperature and precipitation

332   (excluding Antarctica) as derived from the CRU-NCEP data. Both temperature and

333   precipitation show an overall increase over the 20th century that continues into the 21st

334   century, associated with the changing climate.

335

336   The land cover data are used by the model to specify the fractional coverage of CTEM's nine

337   PFTs in each grid cell. These data are based on a geographical reconstruction of the historical

338   land cover driven by the increase in crop area (Arora and Boer, 2010) but using the crop area

339   data based on the LUH2 v1h version of the Hurtt et al (2006) land cover product. The final

340   data set consists of the fractional coverage of CTEM's nine PFTs for the period 1850-2015 at

341   the global scale and at 2.81° spatial resolution. The increase in crop area over the historical

342   period leads to decrease in area of natural vegetation thus leading to deforestation. A fraction

343   of deforested vegetation is burned but deforested biomass is also converted to paper and

344   wood products which decompose over time leading to land use change emissions. These

345   processes are described in detail in Arora and Boer (2010). In context of terrestrial methane

346   budget, an increase in crop area leads to lower methane uptake by soil over the cultivated

347   fraction of a grid cell.

348

349   The globally averaged atmospheric CO_2 and CH_4 concentrations used to drive the model are

350   obtained from the data sets put together for the sixth phase of the Coupled Model

351   Intercomparison Project (CMIP6) and available from input4MIPs web site (https://esgf-

352   node.llnl.gov/projects/input4mips/). These data are shown in Figure B2.

2.1.3 Observation and model-based data for CLASS-CTEM evaluation

In addition to evaluating the CLASS-CTEM simulated methane emissions from wetlands, fire and methane uptake by soils in the context of the one-box atmospheric CH_4 model as mentioned in section 2.2 below, we also evaluate simulated present-day wetland extent and all modelled methane fluxes directly against other model and observation-based estimates.

The CLASS-CTEM simulated wetland extent is compared against two data sets: the wetland data from the Global Lakes and Wetlands Database (GLWD; Lehner and Döll, 2004) and a new product that is formed by merging remote sensing based observations of daily surface inundation from the Surface Water Microwave Product Series (SWAMPS; Schroeder et al., 2015) with the static inventory of wetland area from the GLWD. The derivation of the second product is explained in detail in Poulter et al. (2017). SWAMPS provides estimates of fractional surface water based on data from multiple passive and active microwave satellite missions. While open water (e.g. rivers, lakes and ocean) and inundated wetlands comprising of open plant canopies are mapped by satellites, inundation beneath closed forest canopies, and exposed wetlands with water table below the surface cannot be mapped. However, satellite data are able to provide the seasonal cycle which static data sets like GLWD cannot. The merged SWAMPS-GLWD product attempts to overcome limitations of both individual data sets.

The simulated present-day methane emissions from wetlands and fire, and methane uptake by soil, are compared to top-down estimates compiled by Saunois et al. (2016). We also compare the anthropogenic emissions we have used within the framework of one-box atmospheric methane model (Section 2.2) with estimates from Saunois et al. (2016).

379   Finally, we also evaluate the model regionally over the West Siberian Lowlands (WSL). This

380   region is chosen because inversion-based methane fluxes are readily accessible over the

381   region which were compiled and documented for the WETCHIMP-WSL Intercomparison

382   project (Bohn et al., 2015). We compare simulated wetland extent and wetland methane

383   emissions with observation- and inversion-based results from Bousquet et al. (2011), Kim et

384   al. (2011), and Winderlich (2012) and participating models in the Wetland and Wetland CH_4

385   Intercomparison of Models Project (WETCHIMP, Melton et al. (2013)) focused on the West

386   Siberian Lowlands region (WETCHIMP-WSL) (Bohn et al., 2015). Of these the Kim et al.

387   (2011) and Winderlich (2012) are regional inversions. Kim et al. (2011) used wetland

388   methane emissions from Glagolev et al. (2010) at 1° spatial resolution as their prior and used

389   the NIES-TM atmospheric transport model for the period 2002–2007. They derived

390   climatological monthly wetland emissions optimized to match atmospheric methane

391   concentrations obtained by aircraft sampling. Winderlich (2012) used the Kaplan (2002)

392   wetland inventory for prior wetland emissions with the TM3-STILT global inversion system

393   for year 2009. Their posterior monthly wetland emissions were uniquely determined for each

394   grid cell within their domain at 1° spatial resolution and optimized to match atmospheric

395   methane concentrations measured at four tower observation sites located between 58°N and

396   63 °N. The Bousquet et al. (2011) is a global inversion but uses two priors – the first one

397   based on the Matthews and Fung (1987) emissions inventory and the second based on Kaplan

398   (2002). Bousquet et al. (2011) inversion used the Laboratoire de Météorologie Dynamique

399   general circulation model (LMDZ) atmospheric transport model at a 3.75° × 2.5° grid and

400   estimated monthly methane emissions at a 1° spatial resolution for the period 1993–2009.

401   Being a global inversion they optimized atmospheric concentrations relative to global surface

402   observations at several flask stations for methane but also other trace gases. For wetland

403   extent, we compare the CLASS-CTEM simulated wetland extent over the WSL region with

404   models participating in the WETCHIMP-WSL intercomparison, and GLWD and

405   SWAMPS+GLWD products mentioned above but also the Global Inundation Extent from

406   Multi-Satellites (GIEMS; Papa et al., 2010; Prigent et al., 2007) derived from visible and

407   near-infrared and active and passive microwave sensors for the period 1993–2004. In

408   addition, we also use the estimate from Peregon et al., (2009) who used a regional wetland

409   typology map further refined by satellite image classifications to calculate the wetland extent

410   in the WSL region.

411   **2.2 Atmospheric methane – one box model, anthropogenic emissions and lifetime**

412   **2.2.1 One-box model of atmospheric methane**

413

414   A one-box model of atmospheric CH_4 is used to evaluate the time evolution of simulated

415   methane emissions from wetlands (E_w), methane emissions from fire (E_f) and the soil uptake

416   of methane (S_{soil}) over the period 1850-2008. The model describes the changes in burden of

417   atmospheric CH_4 (B) as a balance of surface emissions (consisting of natural, E_N, and

418   anthropogenic emissions, E_A) and the atmospheric (S_{atmos}) and surface soil sinks (S_{soil}).

419 $$\frac{dB}{dt} = E_N(t) + E_A(t) - S_{atmos}(t) - S_{soil}(t) \tag{3}$$

420   where *t* is the time and equation (3) is applied at an annual time step. The atmospheric CH_4

421   burden (B, Tg CH_4) equals 2.78 times [CH_4] (represented in units of parts per billion, ppb)

422   (Denman et al., 2007). The distinction between natural and anthropogenic emissions is not

423   straight-forward for fire which contains emissions due to both natural and human-caused

424   fires. For comparison with Saunois et al. (2016) global CH_4 budget (as shown later in Section

425   3) we consider all emissions from fire as anthropogenic, although the CLASS-CTEM model

426   calculates fire emissions due both to lightning and human-caused ignitions. Natural emissions

427   ($E_N = E_w + E_o$) consist of modelled wetlands emissions (E_w) and emissions from other

428   natural sources (E_o) (including termites, geological sources, wild animals and freshwater)

429   which we specify at 25 Tg CH₄/yr (consistent with but towards the lower end of the range

430   natural emissions, 21-130 Tg CH₄/yr, as deduced by top-down approaches summarized in

431   Saunois et al. (2016)). The reason for specifying E_o at 25 Tg CH₄/yr is discussed later in

432   section 4. Anthropogenic emissions ($E_A = E_{A\,\text{excl fire}} + E_f$) consist of specified emissions

433   from all anthropogenic sources excluding fire ($E_{A\,\text{excl fire}}$) and fire emissions which we

434   explicitly model (E_f). Estimation of anthropogenic emissions excluding those from fire and

435   biomass burning ($E_{A\,\text{excl fire}}$) data are explained in section 2.2.2.

436

437   The atmospheric sink S is calculated as a first-order loss process from methane's lifetime

438   τ_{chem} in the atmosphere as $S_{atmos}(t) = B(t)[1 - \exp(-1/\tau_{chem}(t))]$. An estimate of τ_{chem}

439   is obtained from the Canadian Middle Atmosphere Model (CMAM) with chemistry and

440   compared to an observation-based estimate from Prather et al. (2012) as later shown in

441   Section 2.2.3. With S_{atmos} represented in terms of τ_{chem} equation (4) can be rewritten as

442

$$
\begin{aligned}
B(t + \Delta t) = \ & B(t) - B(t)[1 - \exp(-1/\tau_{chem}(t))] + \big(E_N(t) + E_A(t) - S_{soil}(t)\big)\Delta t \\
= \ & B(t)[\exp(-1/\tau_{chem}(t))] + \big(E_N(t) + E_A(t) - S_{soil}(t)\big)\Delta t
\end{aligned}
\tag{4}
$$

444

445   where Δt = 1 year. Equation (4) can be used to evaluate simulated natural methane emissions

446   E_N in two ways. First, when all the terms on the right hand side of equation (4), including an

447   initial value of $B(t)$, are known then the time evolution of B can be calculated and compared

448   to its observation-based estimate. Second, if the time evolution of B is specified based on

449   observations of methane concentration in the atmosphere then the value of τ_{chem} required to

450   satisfy equation (4) can be calculated (see equation 5) and compared its observation-based

451   estimate e.g. from Prather et al. (2012).

452    $$\tau_{chem}(t) = -\frac{1}{log\left(\frac{B(t+\Delta t)-\left(E_N(t)+E_A(t)-S_{soil}(t)\right)\Delta t}{B(t)}\right)}$$ (5)

453

454   In section 3, we have used both these methodologies to assess CLASS-CTEM simulated

455   methane emissions from wetlands (E_w), methane emissions from fire (E_f) and the soil uptake

456   of methane (S_{soil}). Note that equation (4) does not include any term for oceanic methane

457   emissions. Saunois et al. (2016) report a range of 0–5 Tg CH_4/yr, with a mean value of 2 Tg

458   CH_4/yr for oceanic methane emissions. Given the large uncertainty in other components of

459   the global methane budget, and the small magnitude of oceanic methane emissions, we have

460   ignored this term.

461

462   Equation (3) may also be used to calculate pre-industrial methane concentration assuming

463   atmospheric methane concentration was in equilibrium with pre-industrial emissions and

464   sinks, i.e. by setting $\frac{dB}{dt} = 0$, which yields

465    $$E_N(t) + E_A(t) = S_{atmos}(t) + S_{soil}(t).$$ (6)

466   Substituting $S_{atmos}(t) = B(t)[1 - \exp(-1/\tau_{chem}(t))]$ similar to as was done in equation

467   (4) and solving for $B(t)$ gives

468    $$B(t) = \frac{E_N(t)+E_A(t)-S_{soil}(t)}{1-\exp(-1/\tau_{chem}(t))}.$$ (7)

469   Using values of sources and sinks and τ_{chem} corresponding to year 1850, for example, yields

470    $B(t)$ (Tg CH_4) which when divided by 2.78 yields [CH_4] in ppb for year 1850.

2.2.2 Anthropogenic methane emissions

The time evolution of global E_A (used in equation 4) for the 1850-2008 period is based on two data sets. The first data set is the decadal representative concentration pathway (RCP) anthropogenic methane emissions data set (version 2.0.5) available at 0.5° spatial resolution for the period 1850-2000 and provided for the fifth phase of the coupled model Intercomparison project (CMIP5) by the International Institute for Applied Systems Analysis (IIASA) (http://www.iiasa.ac.at/web-apps/tnt/RcpDb). The value for the first year of each decade is assumed to correspond to the rest of the decade. So the 1850 value corresponds to the 1850-1859 decade, the 1860 value corresponds to the 1860-69 decade and so on. The second anthropogenic methane emissions data set is part of version 4.2 of the Emission Database for Global Atmospheric Research (EDGAR, http://edgar.jrc.ec.europa.eu/overview.php?v=42) available at 0.1° spatial resolution and available for the period 1970-2008. These data sets were selected because the RCP data set provides the anthropogenic methane emissions going back to 1850 and the EDGAR data set provides the anthropogenic methane emissions for more recent years since 1970. The EDGAR data set was also chosen because amongst the recent anthropogenic data sets this is the only data set which provides gridded anthropogenic methane emissions at an annual time scale (see Table 1 of Saunois et al (2016)).

These two data sets are blended (or harmonized) to obtain a consistent time series of annual global anthropogenic methane emissions for the period 1850-2008. First the RCP and EDGAR data are regridded from their 0.5° and 0.1° spatial resolutions, respectively, to the 2.81° resolution at which the model is applied. Next all non-biomass burning emission categories are added separately in both data sets to obtain total anthropogenic emissions for each data set. The emissions categories in both data sets are somewhat different as shown in

497   Table 2. Emissions from fire and biomass burning are excluded because CLASS-CTEM

498   simulates CH_4 emissions from fire explicitly. Since our framework requires only total

499   anthropogenic methane emissions (excluding biomass burning) the different emissions

500   categories in the two data sets do not matter. The wetland emissions from rice paddies, which

501   we do not explicitly model, are included in the specified anthropogenic emissions (in

502   category 11 of the EDGAR data set and category 1 of the RCP data set as shown in Table 2).

503   Equation (8) summarizes this harmonization methodology for a given grid cell.

504

505    $$E_{A,\text{RCP adjusted}}(t) = E_{A,\text{RCP}}(t) + \frac{t-1850}{1970-1850}\left(E_{A,\text{EDGAR}}(1970) - E_{A,\text{RCP}}(1970)\right) \qquad (8)$$

506

507   where $E_{A,\text{RCP}}$ and $E_{A,\text{EDGAR}}$ represent annual anthropogenic methane emissions (excluding

508   biomass buring) in the RCP and EDGAR data sets, respectively, $E_{A,\text{RCP adjusted}}$ represent the

509   adjusted RCP emissions and t is the time in years from 1850 to 1970. The harmonization

510   algorithm adjusts the annual total anthropogenic methane emissions in the RCP data, for each

511   2.81° grid cell, from 1850 to 1970 such that by the time RCP emissions reach 1970 they are

512   the same as the EDGAR's total emissions excluding biomass burning. As a result of this

513   harmonization, the largest change is made to RCP emissions for year 1970 and the smallest

514   change is made for year 1851. The RCP emissions for year 1850 are not changed. The final

515   harmonized time series for E_A is obtained by concatenating $E_{A,\text{RCP adjusted}}$ for the period 1850

516   to 1970 and $E_{A,\text{EDGAR}}$ for the period from 1971 to 2008.

517

518   Figure 1a shows the harmonized time series of global anthropogenic methane emissions

519   along with the decadal RCP and annual EDGAR emissions (excluding biomass burning). The

520   RCP and EDGAR emissions are fairly similar for the period 1970-1990 but are different after

521   1990. Figures 1b and 1c illustrate how the harmonization works for two selected grid cells

522 based on equation (8). In Figure 1b anthropogenic methane emissions are shown for a land

523 grid cell where emissions first increase and then decrease. In Figure 1c anthropogenic

524 methane emissions are shown for an ocean grid cell, with six orders of magnitude lower

525 emissions than the land grid cell, where emissions more or less continuously increase. In both

526 case, the harmonization ensures that by 1970 the adjusted RCP emissions are same as the

527 EDGAR emissions. Although for the purpose of using E_A in equation (4) only its global

528 values are required, the methodology described here yields a continuous consistent gridded

529 data set of anthropogenic methane emissions for the period of our analysis with no abrupt

530 jumps.

531
532 **2.2.3 Lifetime of atmospheric methane**
533

534 To use equation (4), for evaluation of CLASS-CTEM simulated annual values of E_w, E_f and

535 S_{soil} over the historical period, time-evolving annual values of τ_{chem} are required. We obtain

536 values of τ_{chem} simulated by the Canadian Middle Atmosphere Model (CMAM). The

537 CMAM is a fully interactive chemistry-climate model (CCM) that is based on a vertically

538 extended version of the third generation Canadian Atmospheric General Circulation Model

539 with a model lid at 95 km (Scinocca et al., 2008). The model contains a description of the

540 important physical and chemical processes of the stratosphere/mesosphere and has been

541 extensively assessed against observations through participation in two phases of the

542 Chemistry-Climate Model Validation (CCMVal) activity (Eyring et al., 2006; SPARC

543 CCMVal, 2010). Of more importance for methane, the chemistry has been extended

544 throughout the troposphere by including cloud corrections on clear-sky photolysis rates,

545 emissions of ozone precursors CO and NO_x (NO + NO_2) including emissions of NO_x from

546 lightning, hydrolysis on specified tropospheric sulphate aerosols and interactive wet and dry

547 deposition. Note that the chemical mechanism currently used in CMAM has not yet been

548 extended to include the chemistry of non-methane hydrocarbons important in the

549 troposphere; only methane chemistry is considered.

550

551 Results from CMAM with tropospheric chemistry have been submitted to the Atmospheric

552 Chemistry and Climate Model Intercomparison Project (ACCMIP) (Lamarque et al., 2013).

553 The experimental design for ACCMIP involved timeslice simulations at various points in

554 time between 1850 and 2100, with simulations for year 2000 conditions used for assessing

555 the model chemical climate against available present-day observations. The ACCMIP

556 intercomparison found that the CMAM produced estimates of tropospheric chemical

557 quantities that fell well within the range of current generation CCMs. For example, the

558 present-day tropospheric ozone burden from CMAM was 323 Tg, versus a multi-model mean

559 of 337 ± 23 Tg, where the range is given as one standard deviation across the 15 participating

560 models (Young et al., 2013). The present-day methane lifetime to reaction with OH in the

561 troposphere was found to be 9.4 years, again well within the range of ACCMIP models of 9.7

562 ± 1.5 years (Naik et al., 2013). However, like the majority of ACCMIP models, the CMAM

563 predicts a too fast removal of CH_4 by OH as compared with our best-estimate from methyl-

564 chloroform decay of 11.2 ± 1.3 years (Prather et al., 2012). As described further below, the

565 calculated CH_4 lifetime to chemical loss from CMAM is therefore scaled to agree with

566 observationally-based estimates before being used in the one box atmospheric model of CH_4.

567

568 Time-dependent values of τ_{chem} are derived from a simulation over the 1850-2014 period

569 that uses specified sea-surface temperatures and sea-ice from one member of the five-member

570 historical ensemble performed by CanESM2 for the CMIP5. Data for 2006-2014 was taken

571 from a continuation of that simulation for the RCP 6.0 scenario. Specified anthropogenic and

572 biomass burning emissions of CO and NO_x were taken from the CMIP5 historical database

573 (Lamarque et al., 2010) up to 2000 and for the RCP 6.0 scenario to 2014. Specified

574 concentrations of long-lived greenhouse gases were from Meinshausen et al. (2011),

575 following RCP 6.0 from 2006-2014. Specified stratospheric aerosol surface area density

576 fields, used to account for the effects of large volcanic eruptions, was based on the 1960-2010

577 database created for the Chemistry Climate Model Initiative (CCMI) extended back to 1850

578 following the approach described in Neely III et al. (2016). Solar variability was included by

579 calculating the wavelength-resolved daily variability relative to the long-term average (June

580 1976 – January 2007) from the recommended CMIP6 database (Matthes et al., 2017).

581

582 The observation-based estimate of τ_{chem} is obtained from Prather et al. (2012) who calculate

583 τ_{CH_4} based on equation (9) as

584
$$\frac{1}{\tau_{CH_4}} = \frac{1}{\tau_{OH}} + \frac{1}{\tau_{strat}} + \frac{1}{\tau_{trop-Cl}} + \frac{1}{\tau_{soil}} = \frac{1}{\tau_{chem}} + \frac{1}{\tau_{soil}} \tag{9}$$

585 where τ_{OH} (present day value of 11.2 years), τ_{strat} (120 years), $\tau_{trop-Cl}$ (200 years) and τ_{soil}

586 (150 years) are the lifetimes associated with the destruction of CH_4 by tropospheric OH

587 radicals, loss in the stratosphere, reaction with tropospheric chlorine and uptake by soils,

588 respectively, which yields a present day (corresponding to year 2010) value of τ_{CH_4} as

589 9.1±0.9 years. τ_{chem} is the methane life time associated with chemical processes in the

590 atmosphere. For the pre-industrial period (corresponding to year 1750), Prather et al. (2012)

591 estimate τ_{CH_4} as 9.5±1.3 years assuming τ_{OH} to be equal to 11.76 years (based on

592 Atmospheric Chemistry and Climate Model Intercomparison Project (ACCMIP) results

593 (Voulgarakis et al., 2013)) and lifetimes associated with other processes are assumed to stay

594 the same. In our study, the methane soil sink is explicitly simulated in the CLASS-CTEM

595   framework and this corresponds to the term $\frac{1}{\tau_{soil}}$ in equation (9). The remaining terms in

596   equation (9) all correspond to atmospheric processes. Removing the $\frac{1}{\tau_{soil}}$ term in equation (9)

597   gives us an observation-based estimate of τ_{chem} making it consistent with CMAM's methane

598   lifetime corresponding only to atmospheric processes and increases the observation-based

599   estimates of pre-industrial and present-day atmospheric CH_4 lifetimes to 10.15±1.45 years

600   and 9.7±1.0 years, respectively.

601

602   Figure 2 compares the τ_{chem} values from CMAM with its observation-based estimate from

603   Prather et al. (2012) and shows that CMAM based estimates are biased low and outside the

604   uncertainty range of observation-based estimates, as mentioned earlier. When used in the

605   one-box model of atmospheric methane, the lower than observed τ_{chem} values will

606   inevitably lead to a higher than observed atmospheric sink (S_{atmos}) and thus lower than

607   observed atmospheric methane concentration even if all the other flux terms (E_N, E_A, and

608   S_{soil}) in equation (5) are realistic. We therefore adjust the CMAM derived values of τ_{chem}

609   upwards by 15% so that they lie within the uncertainty range of observation-based estimates

610   of the τ_{chem} as derived by Prather et al. (2012). These adjusted values of τ_{chem} are also

611   shown in Figure 2.

612

613   **2.3 The experimental setup**

614

615   **2.3.1 Equilibrium pre-industrial simulation**

616

617   The equilibrium pre-industrial simulation was initialized from zero biomass for all PFTs. The

618   fractional coverages of CTEM's nine PFTs for the pre-industrial simulation are based on the

619 land cover product described in section 2.1.2 for year 1850. The model was then driven with

620 1901-1925 CRU-NCEP climate data cycled repeatedly until the model pools reach

621 equilibrium. The early part of the 20th century does not show any significant trends compared

622 to the later part of the 20th century, as seen in Figure B1 (Appendix B), so using the 1901-

623 1925 data to spin up the model to equilibrium for 1850 conditions is reasonable. Atmospheric

624 CO_2 and CH_4 concentration levels were set to 285 ppm and 791 ppb, respectively,

625 corresponding to their pre-industrial 1850 levels. This pre-industrial equilibrium simulation

626 yields initial conditions for all CLASS-CTEM prognostic variables for the transient 1851-

627 2015 simulation.

628

629 **2.3.2 Transient historical simulation**

630

631 The transient historical simulation is performed for the period 1851-2015 and its prognostic

632 variables are initialized from the equilibrium pre-industrial simulation as mentioned above.

633 For the period 1851 to 1900 of this simulation the model is driven with meteorological data

634 from 1901-1925 twice similar to what was done for spinning up the model for the pre-

635 industrial simulation. For the period 1901-2015 the meteorological data corresponding to

636 each year are used. Time varying concentrations of atmospheric CO_2 and CH_4 are specified

637 for the period 1851-2015. The annual time-varying fractional coverages of C_3 and C_4 crop

638 PFTs in each grid cell are based on LUH2 v1h version of the Hurtt et al (2006) land cover

639 product.

640

641 In this transient simulation, 1) wetland extent and its methane emissions respond to changes

642 in climate but also increases in atmospheric CO_2 concentration (which increases net primary

643 productivity and thus heterotrophic respiration), 2) methane emissions from fire respond to

644 changes in climate, atmospheric CO_2 concentration, population density and land use change,

645 and 3) methane uptake by soil responds to climate, changes in atmospheric CH_4 concentration

646 and changes in crop fraction.

647

648 **3. Results**

649

650 We first show the results from the transient 1851-2015 simulation and evaluate the time-

651 evolution of CLASS-CTEM simulated global natural methane fluxes over the historical

652 period using the one-box model of atmospheric methane described in section 2.2. This is

653 followed by evaluation of model fluxes for the present day against observation-based

654 estimates and for the WSL region using observation-based estimates and results from other

655 models.

656

657 **3.1 Time evolution of simulated global natural methane fluxes**

658

659 Figure 3 shows the time evolution of simulated annual maximum wetland extent, methane

660 emissions from wetlands and fire, and soil uptake by methane from the 1851-2015 transient

661 historical simulation. In Figure 3: 1) the simulated wetland methane emissions increase by

662 30% over the historical period from about 130 to 169 Tg CH_4/yr from 1850s to the present

663 day (2000-2008) partly due to increase in wetland extent which increases by 8% from 7.5 to

664 8.1 million km^2 from 1850s to the present day, 2) the simulated fire methane emissions

665 decrease from their 1850s value by 20% from about 34 to 27 Tg CH_4/yr for the present day

666 and 3) the soil methane uptake more than doubles from its 1850s value of about 14 to 29 Tg

667 CH_4/yr for the present day.

668

669 The increase in wetland methane emissions over the historical period is due to an increase in

670 the wetland area, driven by increase in precipitation seen in Figure B1 (Appendix B), but also

671 higher methane fluxes per unit area. The higher methane fluxes per unit area are caused by

672 increase in atmospheric CO_2 concentration which increases both net primary productivity and

673 heterotrophic respiration over the historical period as shown in Figure C1 in Appendix C.

674 Since wetland methane emissions are proportional to heterotrophic respiration (R_h) in

675 equation (2) an increase in R_h also increases methane emissions from wetlands.

676

677 The decrease in methane emissions from wildfires is driven by a decrease in area burned

678 which itself is driven by an increase in crop area and population density over the historical

679 period (Arora and Melton, 2018). The increase in cropland area decreases area burned by

680 wildfires in the model since croplands are not allowed to burn. In the real world cropland area

681 also fragments the landscape which affects the spread of fire. Direct anthropogenic influences

682 on wildfires are more complex since accidental, as well as intentional, human-caused

683 ignitions enhance wildfires while anthropogenic suppression of wildfires decreases area

684 burned and fire related emissions. Figure C2 (Appendix C) shows that the overall effect of

685 increase in crop area and population density in the model is that area burned increases

686 slightly up to about 1930, and then starts decreasing thereafter and this area burned pattern

687 compares reasonably with the decadal charcoal index from the Global Charcoal Database

688 version 3 (Marlon et al., 2008) for the full length of the historical simulation. Winds and

689 smoke carry charcoal from fires and deposit it onto aquatic sediments and this forms the basis

690 of sediment charcoal indices. The caveat with the comparison with sediment charcoal records

691 is that they provide only a proxy for fire activity and indicate if fire activity is higher or lower

692 relative to a point in time. Figure C2 also compares area burned with estimates from version

693   4.1s of the Global Fire Emissions Database (Giglio et al., 2013; Randerson et al., 2012) that

694   are based on the satellite record and available only for the short 1997-2014 period. Model and

695   observation-based average burned area over this 1997-2014 period are 483.4 and 485.5

696   million hectares year^{-1} and their trends are –5.57±1.25 and –3.43±1.05 million hectares year^{-}

697   ^{2}, respectively. The negative trends indicate burned area has been decreasing.

698

699   Finally, the increase in methane uptake by soils is primarily the response to an increase in the

700   atmospheric concentration of methane. Diffusion of methane into the soil is directly

701   proportional to its atmospheric concentration (Curry, 2007) which more than doubles from

702   around 790 ppb in 1850 to around 1830 ppb in 2015 (Figure B2, panel b).

703

704   **3.2 Evaluation of simulated global natural methane fluxes**

705

706   We first evaluate the CLASS-CTEM simulated global natural methane fluxes in a forward

707   simulation where all the right hand side terms of equations (3) and (4) are specified at an

708   annual time step and the change in atmospheric methane burden $\frac{dB}{dt}$ is calculated every year.

709   Although the CRU-NCEP meteorological data are available to 2015 allowing us to perform

710   offline CLASS-CTEM simulations up until 2015, the last year for which harmonized RCP-

711   EDGAR emissions are available is 2008. We therefore simulate the time evolution of

712   atmospheric methane concentration for the period 1851-2008. In this forward calculation of

713   atmospheric methane burden the one box model may be initialized using the observed 1850

714   methane concentration or using the 1850 concentration that is in equilibrium with 1850 sinks

715   and sources. The latter is calculated by assuming $\frac{dB}{dt} = 0$ as illustrated in equations (6) and

716   (7). The numerator term in equation (7) $(E_N(t) + E_A(t) - S_{soil}(t))$ for year 1850 is 214.2 Tg

717   CH$_4$/year (wetland emissions are 130.1, other natural emissions are specified at 25,

718   anthropogenic emissions are 39.5, fire emissions are 33.2, and soil uptake is 13.6). In

719   equation (7) using adjusted CMAM τ_{chem} value of 8.82 years (for year 1850, red line in

720   Figure 2) yields an 1850 equilibrium [CH$_4$] for 1850 of 719 ppb compared to its observation-

721   based value of 791 ppb. In contrast, using the midrange value of τ_{chem} of 9.97 years based on

722   Prather et al. (2012) yields equilibrium [CH$_4$] for 1850 of 808 ppm which compares much

723   better with its observation-based estimate of 791 ppm. An equilibrium methane concentration

724   in 1850 that is lower than observed, when using adjusted CMAM τ_{chem}, implies that the

725   atmospheric methane sink is higher and associated with lower than observed atmospheric

726   methane lifetime in 1850. Indeed, the adjusted CMAM τ_{chem} for 1850 of 8.82 years is less

727   than Prather et al. (2012) midrange estimate of 9.97 years but still within their uncertainty

728   range as seen in Figure 2. Regardless, since the lifetime of methane in the atmosphere is only

729   around 10 years the effect of initial conditions disappears by around 1870. This is shown in

730   Figure 4a which compares the simulated evolution of atmospheric methane burden with its

731   observations using the adjusted CMAM τ_{chem}. Figure 4a shows that overall the simulated

732   increase in methane concentration over the historical period is reasonable compared to

733   observation-based estimates despite the various specified and modelled sources and sinks that

734   contribute to the time evolution of atmospheric methane burden. In Figure 9a, the coefficient

735   of correlation between observation-based (black line) and simulated (green and blue lines)

736   [CH$_4$] is 0.99 and root mean square error (RMSE) is 35 ppb (green line) and 41 ppb (blue

737   dashed line). The simulated values are somewhat overestimated from 1885 to 1980 and

738   underestimated from 1980 to 2005. The increase in observed methane concentration over the

739   1850 to 2008 period is 998 ppb, while the one box model yields an increase of 1006 ppb

740   when initialized from observed 1850 methane concentration. The year 2008 concentration is

741   calculated to be 1797 ppb compared to the observation-based value of 1790 ppb.

742

743   An alternative approach to evaluate the modelled natural sinks and sources is to specify the

744   rate of increase of atmospheric methane burden according to its observations and calculate

745   the required atmospheric lifetime of methane (excluding the soil sink), given modelled

746   natural sinks and sources, following equation (5) as discussed in section 2.2. These results are

747   shown in Figure 4b, which compares the methane lifetimes required to achieve the observed

748   increase in methane concentration over the historical period (black line) to within ± 3 ppb

749   (shaded area between grey lines) with observation-based estimate of atmospheric methane

750   lifetime based on Prather et al. (2012) and the adjusted atmospheric methane lifetime from

751   CMAM (both of which were shown earlier in Figure 2). Figure 4b shows that for the most

752   part, the calculated atmospheric methane lifetime stays within the uncertainty of observation-

753   based estimates. More over the temporal trend after 1900 in calculated atmospheric methane

754   lifetime compares well to the trend in the atmospheric methane lifetime from the CMAM

755   model. Both anthropogenic emissions and methane concentration during the early part of the

756   1850-2008 historical period are more uncertain than during the later part and therefore the

757   differences between simulated and observation-based estimates of atmospheric methane

758   concentration (in Figure 4a) and methane lifetimes (in Figure 4b) for the period 1850-1900

759   are not unexpected.

760

761   While the results in Figures 4a and 4b provide some confidence that the magnitude and

762   temporal evolution of simulated global natural methane sources and sinks over the historical

763   period are reasonable they, of course, do not allow the evaluation of all of the simulated

764   natural fluxes individually.

765

766 We also evaluate the role of increase in wetland methane emissions over the historical period

767 (as seen in Figure 3) on the historical methane budget. Instead of using wetland methane

768 emissions from the transient historical simulation in the one box model of atmospheric

769 methane we use wetland methane emissions from the equilibrium pre-industrial simulation in

770 which 1901-1925 CRU-NCEP meteorological data are used repeatedly and CO_2 is held

771 constant at its pre-industrial level of 285 ppm. As a result wetland extent and methane

772 emissions do not respond to changes in climate and increasing CO_2, and do not increase over

773 the historical period (as seen in Figure 5a). Methane emissions from fire and soil uptake of

774 methane still respond to changes in climate and increasing CO_2. The result of using these

775 wetland methane emissions (shown in Figure 5a) in the framework of the one box model of

776 atmospheric methane is shown in Figure 5b. In Figure 5b, although [CH_4] overall increases

777 over the historical period in response to increase in anthropogenic emissions, the result of

778 wetland methane emissions not increasing over the historical period is that the simulated

779 atmospheric methane concentration in year 2008 is calculated to be 1667 ppm, which is 130

780 ppb lower than the 1797 ppb seen in Figure 4a.

781
782 **3.3 Geographical distribution of wetland extent**

783

784 Figure 6 compares the zonally-averaged maximum wetland fraction over land with

785 observation-based estimates based on the Global Lakes and Wetland (GLWD; Lehner and

786 Döll, 2004) and the new product formed by merging remote sensing based observations of

787 daily surface inundation from the Surface Water Microwave Product Series (SWAMPS;

788 Schroeder et al., 2015) with the static inventory of wetland area from the GLWD from

789 Poulter et al. (2017), as mentioned earlier in section 2.1.3. Maximum wetland fraction from

790 the model and SWAMPS+GLWD product is calculated as the maximum of 12 mean monthly

791 values from the 13 years spanning the 2000-2012 period. Figure 6 shows that overall the

792 model is able to capture the broad latitudinal distribution of wetlands with higher wetland

793 fraction at northern high-latitudes and in the tropics. The model yields higher wetland

794 fraction in the tropics than both observation-based estimates and this is due to higher wetland

795 fraction simulated in the Amazonian region. The Amazonian region is densely forested and

796 the SWAMPS product is unable to map wetlands beneath closed forest canopies. Biases also

797 likely exist in the GLWD data set since parts of the Amazonian region are fairly remote. This

798 is shown in Figure 7 which compares the geographical distribution of simulated maximum

799 wetland fraction with that from the GLWD and SWAMPS+GLWD products. The model

800 successfully captures wetlands in the Hudson Bay lowlands, the West Siberian lowlands, the

801 Pantanal and the region bordering Argentina, Paraguay and Uruguay in South America,

802 Indonesia and the low lying region around Bangladesh. In terms of differences from these

803 observation-based data sets the model most notably overestimates wetland extent in Europe.

804 One possible reason for this is that wetlands in Europe have been drained for agriculture and

805 our wetland parameterization does not take this into account. About two-thirds of the

806 European wetlands that existed 100 years ago have been lost (European Commission, 1995)

807 leading to a substantial decrease in the number and size of large bogs and marshes, and small

808 or shallow lakes.

809

810 **3.4 Geographical distribution of simulated natural fluxes**

811

812 Figure 8 shows the geographical distribution of methane emissions from dynamic wetlands

813 (panel a) and fire (panel b) and the soil uptake of methane (panel c) simulated by the CLASS-

814 CTEM model. The figures also show the global total of these fluxes averaged over the 2000-

815 2008 period for later comparison with estimates from Saunois et al. (2016). Methane

816   emissions from wetlands (168.9 Tg CH_4/yr) are the largest of natural fluxes, as is well

817   known, while emissions from fire (26.8 Tg CH_4/yr) and methane uptake by soil (28.7 Tg

818   CH_4/yr) are an order of magnitude lower. As expected, the geographical distribution of

819   methane emissions from wetlands (Figure 8a) corresponds well to the geographical

820   distribution of wetlands themselves (Figure 8a) although per unit wetland area methane

821   emissions are higher in tropics and milder temperate regions than in high-latitude regions.

822   This is because warmer temperatures and longer growing season in the tropical and milder

823   temperate regions imply that wetlands can emit more methane per unit wetland area and for a

824   longer period of time than the colder high-latitude regions with a shorter growing season. In

825   Figure 8b the geographical distribution of methane fire emissions shows higher values in

826   seasonally-dry tropical regions and order of magnitudes lower values in mid-high latitude

827   regions. These results are consistent with area burned (not shown) which shows a similar

828   pattern (Arora and Melton, 2018). Finally, the geographical distribution of methane uptake by

829   soils in Figure 8c shows higher methane uptake by soils in parts of arid regions (including the

830   Sahara and the Australian outback) where soil moisture doesn't get too dry (so as to not

831   excessively limit soil microbial activity) but otherwise fairly uniform uptake in the tropics

832   and lower values in mid-high latitude regions where lower temperatures and higher soil

833   moisture limit methane uptake by soils.

834

835   **3.5 Regional evaluation over West Siberia lowlands**

836

837   While evaluation of simulated global wetland extent and wetland methane emissions, and

838   their geographical distribution, provides confidence in model results, we further evaluate the

839   model at a regional scale over the West Siberia lowlands. The model results are sampled for

840   the region lying between 50 to 75 °N and 60 to 95°E for comparison with observation- and

841   inversion-based estimates (mentioned earlier in section 2.1.3). Figure 9a compares CLASS-

842   CTEM simulated wetland extent with those from models participating in the WETCHIMP-

843   WSL intercomparison, and the GIEMS, SWAMPS and merged SWAMPS and GLWD

844   products mentioned in section 2.1.3. Table 2 compares the simulated annual maximum

845   wetland extent with models participating in the WETCHIMP-WSL intercomparison and these

846   observation-based products. All values are reported as average for the period 1993-2004

847   except for the merged SWAMPS and GLWD product whose average is for the 2002-2012

848   period, and the Peregon et al. (2009) estimate that is based on wetland typology map from a

849   1977 publication and a more recent satellite land cover product. CLASS-CTEM simulated

850   monthly wetland extent in Figure 9a compares best with the merged SWAMPS and GLWD

851   product, while both the satellite-based inundation products by themselves (SWAMPS and

852   GIEMS) show much lower values. Satellite-based products that remotely sense inundated

853   areas can only do so when water table is above the ground and therefore wetland areas

854   inferred from these products are expected to be lower in magnitude than products which also

855   take into account land cover as is the case for the merged SWAMPS and GLWD product.

856

857   In Table 2, the annual maximum wetland extent is quite similar for the merged SWAMPS

858   and GLWD product (0.55 million km^2) and CLASS-CTEM simulated values (0.53 million

859   km^2) but the maximum occurs in different months. In Figure 9b, for the merged SWAMPS

860   and GLWD product the maximum wetland extent occurs in June while CLASS-CTEM

861   simulated values show peak both in June and September. The participating models from the

862   WETCHIMP-WSL intercomparison show a range of values for the monthly wetland extent in

863   the WSL region (Figure 9a). Models range from those which specify constant values with no

864   seasonality for the wetland extent to models which dynamically model wetland extent two of

865   which show maximum wetland extent of greater than 1 million km^2. The average annual

866   maximum wetland extent across the participating models in the WETCHIMP-WSL is

867 0.70±0.15 million km^2 (mean ± standard error). Finally, the Peregon et al. (2009) estimate is

868 0.68 million km^2 which is somewhat higher than the CLASS-CTEM simulated value (0.53

869 million km^2) and the merged SWAMPS and GLWD product (0.55 million km^2).

870

871 Figure 9b compares CLASS-CTEM simulated monthly wetland methane emissions with

872 those from models participating in the WETCHIMP-WSL intercomparison and four

873 inversion-based estimates mentioned in section 2.1.3. The two Bousquet et al. (2011)

874 inversions shown in Figure 9b correspond to ones using the reference Matthews and Fung

875 (1987) emissions inventory (Bousquet 2001 R) and the emissions inventory based on Kaplan

876 (2002) (Bousquet 2001 K). All values are reported as average for the period 1993-2004

877 except for the Kim et al. (2011) inversion which reports fluxes for year 2005 and the

878 Winderlich (2012) inversion which corresponds to year 2009.

879

880 Table 2 compares the simulated annual wetland methane emissions from CLASS-CTEM with

881 those from models participating in the WETCHIMP-WSL intercomparison and the four

882 inversion-based estimates. In Table 2, the inversion-based annual wetland methane emissions

883 vary from 3.08 to 9.80 Tg CH$_4$/yr. The highest annual emissions in the Winderlich (2012)

884 inversion are due to higher emissions in the shoulder months of spring and fall compared to

885 other inversions but also non-zero emissions during winter months (December to February)

886 as seen in Figure 9b. The CLASS-CTEM model calculates annual wetland methane

887 emissions of 7.76 Tg CH$_4$/yr and the average for models participating in the WETCHIMP-

888 WSL intercomparison is 5.34±0.54 Tg CH$_4$/yr (mean ± standard error). Of all the models and

889 inversions only the Winderlich (2012) inversion shows substantial methane emissions for the

890 November to April period. In CLASS-CTEM as the liquid soil moisture in the top soil layer

891 freezes wetland extent contracts to zero (Figure 9a) and methane emissions are shut off

892   during the winter months. Bohn et al. (2015) note that Winderlich (2012) inversion-based

893   estimates may have been influenced by emissions from fossil fuel extraction and biomass

894   burning, although the seasonality of Winderlich (2012) fluxes, with non-zero emissions even

895   in winter, is plausible. Based on year-round eddy flux measurements of methane emissions

896   from an Alaskan Arctic tundra sites Zona et al. (2016) find that cold season (September to

897   May) emissions account for ≥50% of the annual methane flux, with the highest emissions

898   from non-inundated upland tundra. They find a major fraction of cold season emissions occur

899   during the "zero curtain" period, when subsurface soil temperatures are near 0 °C. Langer et

900   al., (2015) report winter emissions from tundra ponds in Siberia as they are freezing during

901   early winter. They analyzed concentrations of methane in bubbles (trapped in the lake ice)

902   which were higher at depths than at the ice surface. So it is entirely plausible that methane

903   emissions occur during transition to winter months which models fail to simulate and most

904   inversions fail to capture.

905

906   **3.6 Evaluation of present-day global methane budget**

907

908   Our final evaluation of simulated global methane budget is against estimates compiled by

909   Saunois et al. (2016) who synthesize several recent studies to summarize the present-day

910   global methane budget. Our global methane budget is based on simulated and specified fluxes

911   and the use of one box model of atmospheric methane. We exclusively evaluate our

912   simulated global methane budget against the top-down approaches presented in Saunois et al.

913   (2016) since estimates from bottom-up approaches are known to yield higher total emissions

914   than those based on top-down approaches as mentioned earlier in the Introduction. The global

915   methane budget based on top-down approaches which are constrained by the atmospheric

916   CH_4 burden and its loss in the atmosphere is considered more reliable than that based on the

917   bottom-up approaches. These comparisons are shown in Table 3. The natural and

918   anthropogenic sources are divided into their broad categories and so are the sinks which are

919   divided into atmospheric and soil sinks. The Saunois et al. (2016) estimates are reported for

920   the period 2000-2009 while the CLASS-CTEM values correspond to the 2000-2008 period

921   since the EDGAR anthropogenic emissions were available only until 2008 at the time of this

922   study and therefore the one box model of atmospheric methane is also run up until 2008. For

923   clarity, Table 3 also identifies which fluxes are modelled by CLASS-CTEM, which are

924   specified and which are based on atmospheric methane lifetimes.

925

926   In Table 3 the total emissions from natural sources in our framework are 199 Tg CH_4/yr

927   which are in the lower part of the range of 194-292 Tg CH_4/yr compiled by Saunois et al.

928   (2016). This is due to lower specified emissions from non-wetland sources. While our

929   modelled emissions from wetlands of 169 Tg CH_4/yr compare well with the Saunois et al.

930   (2016) central estimate of 166 Tg CH_4/yr, our specified emissions from other natural sources

931   (including termites, geological sources and fresh water bodies) of 25 Tg CH_4/yr are near the

932   low end of their range (21-130 Tg CH_4/yr). In contrast, our anthropogenic emissions of 344

933   Tg CH_4/yr (which include emissions from fire for consistency with Saunois et al. (2016)) are

934   higher than Saunois et al. (2016) central estimate of 319 Tg CH_4/yr and towards the higher

935   end of their range (255-357 Tg CH_4/yr). This is due to the use of EDGAR emissions which as

936   Saunois et al. (2016) note are towards the higher end of all data sets of anthropogenic

937   emissions. Our modelled fire emissions of 27 Tg CH_4/yr are lower than Saunois et al. (2016)

938   central estimate of 35 Tg CH_4/yr. One reason for this is that while we include natural and

939   anthropogenic fires in our framework we do not account for biofuel burning. Overall, our

940   emissions from natural sources are 35 Tg CH_4/yr lower, and emissions from anthropogenic

941   sources are 25 Tg CH_4/yr higher, than the Saunois et al. (2016) central estimates. As a result,

942   the sum of natural and anthropogenic emissions (543 Tg CH_4/yr) in our framework is 9 Tg

943   CH_4/yr lower than Saunois et al. (2016) central estimate (552 Tg CH_4/yr).

944

945   The total sink strength is calculated to be 538 Tg CH_4/yr in our framework which compares

946   well with the Saunois et al. (2016) estimate of 546 Tg CH_4/yr. Saunois et al. (2016) do not

947   provide uncertainty ranges for the atmospheric and total sink. The modelled atmospheric (509

948   Tg CH_4/yr) and soil (29 Tg CH_4/yr) sinks in Table 3 also compare well with Saunois et al.

949   (2016) estimates of 514 and 32 Tg CH_4/yr, respectively.

950

951   **4. Discussion and conclusions**

952

953   The offline evaluation of natural methane fluxes simulated by the CLASS-CTEM modelling

954   framework presented here is the first step in making atmospheric methane concentration a

955   prognostic variable in the family of Canadian earth system models. The evaluation is based

956   on comparison of present-day fluxes with existing observation- and model-based estimates

957   compiled by Saunois et al. (2016) but also the historical evolution of atmospheric methane

958   burden and methane's lifetime simulated using a one box model of atmospheric methane.

959   While our simulated and specified present-day global methane budget components lie within

960   the uncertainty range for top-down estimates from Saunois et al. (2016) this also implies that

961   methane emissions from individual sectors for the present-day budget can be increased or

962   decreased within their uncertainty ranges as long as the total emissions stay the same. The

963   time evolution of the atmospheric methane burden over the historical period, however,

964   provides additional constraints than the present-day methane budget. For example, our

965   specified methane emissions of 25 Tg CH_4/yr from other nature sources (E_o) (including

966   termites, geological sources, wild animals and freshwater) are lower than Saunois et al.

967   (2016) central estimate of 68 Tg CH_4/yr, although still within their uncertainty range (21-130

968   Tg CH_4/yr). In the absence of any information about its time evolution we have assumed that

969   E_o remains constant over the historical period. This is a plausible assumption since we do not

970   expect emissions from termites, geological sources, wild animals and freshwater to show a

971   large response to changing environmental conditions over the historical period. Certainly, not

972   as large as we saw for wetland emissions which increased by 40 Tg CH_4/yr over the 1850-

973   2008 period (Figure 3). However, when we use a constant E_o of 68 Tg CH_4/yr in our

974   framework we obtain higher than observed methane concentration throughout the historical

975   period and the year 2008 value is 1953 ppb compared to 1797 ppb that we obtain in Figure 4a

976   (observed methane concentration for 2008 is 1790 ppb). This is shown in Figure 10. Part of

977   the reason for this may be that present-day EDGAR emissions are higher than other estimates

978   as Saunois et al. (2016) note and that's why we had to choose a lower E_o. However, the

979   global harmonized and RCP anthropogenic emissions are fairly similar up until 1990 (see

980   Figure 1a) and therefore had we use RCP based emissions (up until year 2000) we still would

981   have obtained higher than observed atmospheric methane concentrations throughout the

982   historical period when using E_o of 68 Tg CH_4/yr. Our framework cannot accommodate E_o

983   larger than about 25-30 Tg CH_4/yr without overestimating atmospheric methane

984   concentrations throughout the historical period.

985

986   The second constraint provided by the time evolution of the atmospheric methane burden

987   over the historical period is that related to wetland methane emissions. As seen in section 3.2,

988   in the absence of the simulated increase in wetland methane emissions from about 130 to 170

989   Tg CH_4/yr from 1850s to the present day the simulated year 2008 atmospheric methane

990   concentration is about 100 ppb lower than observed (as seen in Figure 5). Assuming our RCP

991   and EDGAR based harmonized anthropogenic emissions and their increase over the historical

992 period is reasonably realistic, this indicates that it is very likely that wetland methane

993 emissions have indeed increased over the historical period in response to changes in climate

994 and increased atmospheric CO_2 concentration. The results in section 3.1 showed that this

995 increase of 30% in wetland methane emissions in driven more by an increase in methane

996 emissions per unit area than the increase in maximum wetland extent, which increased by

997 about 8% over the historical period. The implication of this is that wetland methane

998 emissions will likely keep increasing in the future in response to the increasing atmospheric

999 concentration of CO_2 driven by higher heterotrophic respiration.

1000

1001 The evaluation of simulated wetland extent against the GLWD and the merged SWAMPS

1002 and GLWD product provides confidence that the model is broadly able to reproduce the

1003 geographical distribution of wetlands although, of course, some limitations remain. Over the

1004 WSL region the simulated estimates of wetland extent and wetland methane emissions are

1005 also broadly consistent with observation-based estimates.

1006

1007 The version of the model used here treats its land mask as binary so each grid cell is either

1008 land or ocean/water. While the model is capable of representing inland lakes using a separate

1009 tile (and simulate the resulting impact on energy and water fluxes) this functionality was not

1010 used in this study. In addition, representation of inland lakes requires modelling methane

1011 emissions from their anoxic sediment (Bastviken et al., 2004) and care needs to be taken to

1012 avoid double counting the wetland extent of inland lakes (Thornton Brett et al., 2016).

1013

1014 We have not evaluated the model's wetland methane emissions at the site level against

1015 observations. Wetland methane emissions are known to be spatially highly heterogeneous and

1016 temporally intermittent (e.g. Godwin et al., 2013) and CLASS-CTEM does not represent

1017   physical processes that govern methane emissions at small spatial and temporal scales.

1018   Instead the model is designed for operation at large spatial scales (> 100 km) and

1019   implementation within an Earth system model and as such only temperature, soil moisture

1020   and substrate availability (through heterotrophic respiration) are taken into account. Water

1021   table depth, ebullition, transport through vascular plants, and PFTs specific to wetlands are

1022   not considered in our modelling framework. The corollary of this is that our model cannot be

1023   expected to reproduce wetland methane emissions at a point scale where site specific

1024   processes and conditions including water depth, ebullition, and wetland specific PFTs

1025   become more important. Similar approaches are followed by several large scale models

1026   including a recent attempt by Bloom et al. (2017) who derive wetland methane emissions

1027   using heterotrophic respiration from eight terrestrial ecosystem models.

1028

1029   We have also not evaluated parameter and forcing uncertainties in relation to simulated

1030   methane emissions. However, several aspects of the CLASS-CTEM model have been

1031   evaluated before against observations including photosynthesis, autotrophic and heterotrophic

1032   respiration, allocation of carbon from leaves to stem and root components, dynamic leaf

1033   phenology, fire, and land use change. These aspects of the model have been evaluated at

1034   point (Arora and Boer, 2005a; Melton et al., 2015), regional (Arora et al., 2016; Garnaud et

1035   al., 2015; Peng et al., 2014) and global (Arora and Boer, 2010; Melton and Arora, 2014,

1036   2016) scales. In regards to processes relevant to methane emissions from wetlands (which, of

1037   course, is the largest natural source) heterotrophic respiration and wetland extent are the most

1038   important. Uncertainties in these two quantities will propagate to calculated methane

1039   emissions from wetlands. The majority of increase in wetland methane emissions over the

1040   historical period comes from an increase in heterotrophic respiratory flux due to increase in

1041   gross and net primary productivities in response to increase in atmospheric CO_2

1042 concentration. The rate of increase of simulated gross primary productivity is adjusted in

1043 CLASS-CTEM to obtain realistic land carbon sink from 1960 onwards (Le Quéré et al.,

1044 2018) but also to obtain a realistic amplitude of the annual CO_2 cycle in a fully coupled Earth

1045 system model simulation (Arora and Scinocca, 2016). The response of model's heterotrophic

1046 respiration to soil moisture is expressed as a function of soil matric potential as mentioned

1047 earlier in section 2.1.1.1. This response is based on Griffin (1981) who suggests that the

1048 microbial activity is optimal at an absolute soil matric potential of 0.05 MPa and decreases as

1049 the soil becomes waterlogged near 0.00 MPa or too dry near 1.5 MPa . This parameterization

1050 has been evaluated indirectly at seasonally dry locations in the Amazonia (Melton et al.,

1051 2015).

1052

1053 Our next step to evaluate natural methane fluxes from CLASS-CTEM is to use these fluxes in

1054 an atmospheric transport model to simulate and compare methane concentrations at selected

1055 stations to assess seasonality of simulated wetland methane emissions at large spatial scales

1056 in a somewhat more direct manner. In addition, CLASS-CTEM simulated natural fluxes can

1057 be used as a prior in a methane inversion-based system, together with anthropogenic methane

1058 emissions, to calculate optimized posterior fluxes to which the prior fluxes can be compared.

1059 Although atmospheric inversions-based systems have their own limitations (Houweling et al.,

1060 2017), the objective is to evaluate CLASS-CTEM simulated natural methane fluxes using a

1061 range of available methodologies.

1062

1063 Overall the results presented here suggest that the natural fluxes of methane between the

1064 atmosphere and the land, and the geographical distribution of wetland extent, simulated by

1065 the CLASS-CTEM modelling framework are sufficiently realistic to use the model to study

1066 the changes in natural methane fluxes due to changes in environmental conditions.

1067

1068

1069 **Acknowledgements**

1070

1071 We would like to thank Douglas Chan and Reinel Sospedra-Alfonso for providing comments

1072 on an earlier version of this manuscript. We also thank the two anonymous reviewers for their

1073 comments and our handling editor Alexey V. Eliseev for his time and effort.

1074

1075

References

Amante, C. and Eakins, B. W.: ETOPO1 1 Arc-Minute Global Relief Model: Procedures, Data Sources and Analysis. NOAA Technical Memorandum NESDIS NGDC-24, 19 pp., doi:10.7289/V5C8276M, 2009.

Andreae, M. O. and Merlet, P.: Emission of trace gases and aerosols from biomass burning, Glob. Biogeochem. Cycles, 15(4), 955–966, doi:10.1029/2000GB001382, 2001.

Arora, V. K.: Land surface modelling in general circulation models: a hydrological perspective, PhD thesis, University of Melbourne, Melbourne, Australia., 1997.

Arora, V. K. and Boer, G. J.: A Representation of Variable Root Distribution in Dynamic Vegetation Models, Earth Interact., 7(6), 1–19, doi:10.1175/1087-3562(2003)007<0001:AROVRD>2.0.CO;2, 2003.

Arora, V. K. and Boer, G. J.: A parameterization of leaf phenology for the terrestrial ecosystem component of climate models, Glob. Change Biol., 11(1), 39–59, doi:10.1111/j.1365-2486.2004.00890.x, 2005a.

Arora, V. K. and Boer, G. J.: Fire as an interactive component of dynamic vegetation models, J. Geophys. Res. Biogeosciences, 110(G2), doi:10.1029/2005JG000042, 2005b.

Arora, V. K. and Boer, G. J.: Uncertainties in the 20th century carbon budget associated with land use change, Glob. Change Biol., 16(12), 3327–3348, doi:10.1111/j.1365-2486.2010.02202.x, 2010.

Arora, V. K. and Melton, J. R.: Reduction in global area burned and wildfire emissions since 1930s enhances carbon uptake by land, Nat. Commun., 9(1), 1326, doi:10.1038/s41467-018-03838-0, 2018.

Arora, V. K. and Scinocca, J. F.: Constraining the strength of the terrestrial CO2 fertilization effect in the Canadian Earth system model version 4.2 (CanESM4.2), Geosci. Model Dev., 9(7), 2357–2376, doi:10.5194/gmd-9-2357-2016, 2016.

Arora, V. K., Boer, G. J., Christian, J. R., Curry, C. L., Denman, K. L., Zahariev, K., Flato, G. M., Scinocca, J. F., Merryfield, W. J. and Lee, W. G.: The Effect of Terrestrial Photosynthesis Down Regulation on the Twentieth-Century Carbon Budget Simulated with the CCCma Earth System Model, J. Clim., 22(22), 6066–6088, doi:10.1175/2009JCLI3037.1, 2009.

Arora, V. K., Scinocca, J. F., Boer, G. J., Christian, J. R., Denman, K. L., Flato, G. M., Kharin, V. V., Lee, W. G. and Merryfield, W. J.: Carbon emission limits required to satisfy future representative concentration pathways of greenhouse gases, Geophys. Res. Lett., 38(5), doi:10.1029/2010GL046270, 2011.

Arora, V. K., Boer, G. J., Friedlingstein, P., Eby, M., Jones, C. D., Christian, J. R., Bonan, G., Bopp, L., Brovkin, V., Cadule, P., Hajima, T., Ilyina, T., Lindsay, K., Tjiputra, J. F. and Wu, T.: Carbon–Concentration and Carbon–Climate Feedbacks in CMIP5 Earth System Models, J. Clim., 26(15), 5289–5314, doi:10.1175/JCLI-D-12-00494.1, 2013.

Arora, V. K., Peng, Y., Kurz, W. A., Fyfe, J. C., Hawkins, B. and Werner, A. T.: Potential near-future carbon uptake overcomes losses from a large insect outbreak in British Columbia, Canada, Geophys. Res. Lett., 43(6), 2590–2598, doi:10.1002/2015GL067532, 2016.

1118 Bastviken, D., Cole, J., Pace, M. and Tranvik, L.: Methane emissions from lakes:
1119 Dependence of lake characteristics, two regional assessments, and a global estimate, Glob.
1120 Biogeochem. Cycles, 18(4), doi: 10.1029/2004GB002238, doi:10.1029/2004GB002238,
1121 2004.

1122 Bloom, A. A., Bowman, K. W., Lee, M., Turner, A. J., Schroeder, R., Worden, J. R., Weidner,
1123 R., McDonald, K. C. and Jacob, D. J.: A global wetland methane emissions and uncertainty
1124 dataset for atmospheric chemical transport models (WetCHARTs version 1.0), Geosci Model
1125 Dev, 10(6), 2141–2156, doi:10.5194/gmd-10-2141-2017, 2017.

1126 Bohn, T. J., Melton, J. R., Ito, A., Kleinen, T., Spahni, R., Stocker, B. D., Zhang, B., Zhu, X.,
1127 Schroeder, R., Glagolev, M. V., Maksyutov, S., Brovkin, V., Chen, G., Denisov, S. N.,
1128 Eliseev, A. V., Gallego-Sala, A., McDonald, K. C., Rawlins, M. A., Riley, W. J., Subin, Z. M.,
1129 Tian, H., Zhuang, Q. and Kaplan, J. O.: WETCHIMP-WSL: intercomparison of wetland
1130 methane emissions models over West Siberia, Biogeosciences, 12(11), 3321–3349,
1131 doi:10.5194/bg-12-3321-2015, 2015.

1132 Bousquet, P., Ringeval, B., Pison, I., Dlugokencky, E. J., Brunke, E.-G., Carouge, C.,
1133 Chevallier, F., Fortems-Cheiney, A., Frankenberg, C., Hauglustaine, D. A., Krummel, P. B.,
1134 Langenfelds, R. L., Ramonet, M., Schmidt, M., Steele, L. P., Szopa, S., Yver, C., Viovy, N.
1135 and Ciais, P.: Source attribution of the changes in atmospheric methane for 2006–2008,
1136 Atmos Chem Phys, 11(8), 3689–3700, doi:10.5194/acp-11-3689-2011, 2011.

1137 Chengjin, C., Megan, B., Youshi, W., Fangliang, H., Jacob, W., Jérôme, C. and Lawren, S.:
1138 Does climate directly influence NPP globally?, Glob. Change Biol., 22(1), 12–24,
1139 doi:10.1111/gcb.13079, 2016.

1140 Collins, W. J., Bellouin, N., Doutriaux-Boucher, M., Gedney, N., Halloran, P., Hinton, T.,
1141 Hughes, J., Jones, C. D., Joshi, M., Liddicoat, S., Martin, G., O'Connor, F., Rae, J., Senior,
1142 C., Sitch, S., Totterdell, I., Wiltshire, A. and Woodward, S.: Development and evaluation of
1143 an Earth-System model – HadGEM2, Geosci. Model Dev., 4(4), 1051–1075,
1144 doi:10.5194/gmd-4-1051-2011, 2011.

1145 Curry, C. L.: Modeling the soil consumption of atmospheric methane at the global scale,
1146 Glob. Biogeochem. Cycles, 21(4), doi:10.1029/2006GB002818, 2007.

1147 Dalva, M., Moore, T. R., Arp, P. and Clair, T. A.: Methane and soil and plant community
1148 respiration from wetlands, Kejimkujik National Park, Nova Scotia: Measurements,
1149 predictions, and climatic change, J. Geophys. Res. Atmospheres, 106(D3), 2955–2962,
1150 doi:10.1029/2000JD900500, 2001.

1151 Denman, K. L., Brasseur, G., Chidthaisong, A., Ciais, P., Cox, P. M., Dickinson, R. E.,
1152 Hauglustaine, D., Heinze, C., Holland, E., Jacob, D., Lohmann, U., Ramachandran, S., da
1153 Silva Dias, P. L., Wofsy, S. C. and Zhang, H.: Couplings Between Changes in the Climate
1154 System and Biogeochemistry, in Climate Change 2007: The Physical Science Basis.
1155 Contribution of Working Group I to the Fourth Assessment Report of the Intergovernmental
1156 Panel on Climate Change [Solomon, S., D. Qin, M. Manning, Z. Chen, M. Marquis, K.B.
1157 Averyt, M.Tignor and H.L. Miller (eds.)], pp. 499–587, Cambridge University Press,
1158 Cambridge, United Kingdom and New York, NY, USA., 2007.

1159 European Commission: Wise use and conservation of wetlands. Communication from the
1160 Commission to the Council and the European Parliament, European Commission, Brussels,
1161 Belgium. [online] Available from: http://aei.pitt.edu/4792/1/4792.pdf (Accessed 12 September
1162 2017), 1995.

Eyring, V., Butchart, N., Waugh, D. W., Akiyoshi, H., Austin, J., Bekki, S., Bodeker, G. E., Boville, B. A., Brühl, C., Chipperfield, M. P., Cordero, E., Dameris, M., Deushi, M., Fioletov, V. E., Frith, S. M., Garcia, R. R., Gettelman, A., Giorgetta, M. A., Grewe, V., Jourdain, L., Kinnison, D. E., Mancini, E., Manzini, E., Marchand, M., Marsh, D. R., Nagashima, T., Newman, P. A., Nielsen, J. E., Pawson, S., Pitari, G., Plummer, D. A., Rozanov, E., Schraner, M., Shepherd, T. G., Shibata, K., Stolarski, R. S., Struthers, H., Tian, W. and Yoshiki, M.: Assessment of temperature, trace species, and ozone in chemistry-climate model simulations of the recent past, J. Geophys. Res. Atmospheres, 111(D22), n/a-n/a, doi:10.1029/2006JD007327, 2006.

Friedlingstein, P., Cox, P., Betts, R., Bopp, L., von Bloh, W., Brovkin, V., Cadule, P., Doney, S., Eby, M., Fung, I., Bala, G., John, J., Jones, C., Joos, F., Kato, T., Kawamiya, M., Knorr, W., Lindsay, K., Matthews, H. D., Raddatz, T., Rayner, P., Reick, C., Roeckner, E., Schnitzler, K.-G., Schnur, R., Strassmann, K., Weaver, A. J., Yoshikawa, C. and Zeng, N.: Climate–Carbon Cycle Feedback Analysis: Results from the C4MIP Model Intercomparison, J. Clim., 19(14), 3337–3353, doi:10.1175/JCLI3800.1, 2006.

Friedlingstein, P., Meinshausen, M., Arora, V. K., Jones, C. D., Anav, A., Liddicoat, S. K. and Knutti, R.: Uncertainties in CMIP5 Climate Projections due to Carbon Cycle Feedbacks, J. Clim., 27(2), 511–526, doi:10.1175/JCLI-D-12-00579.1, 2014.

Garnaud, C., Sushama, L. and Verseghy, D.: Impact of interactive vegetation phenology on the Canadian RCM simulated climate over North America, Clim. Dyn., 45(5), 1471–1492, doi:10.1007/s00382-014-2397-9, 2015.

Giglio, L., Randerson, J. T. and van der Werf, G. R.: Analysis of daily, monthly, and annual burned area using the fourth-generation global fire emissions database (GFED4), J. Geophys. Res. Biogeosciences, 118(1), 317–328, doi:10.1002/jgrg.20042, 2013.

Glagolev, M. V., Kleptsova, I. E., Filippov, I. V., Kazantsev, V. S., Machida, T. and Maksyutov, S. S.: Methane emissions from subtaiga mires of Western Siberia: The "standard model" Bc5, Mosc. Univ. Soil Sci. Bull., 65(2), 86–93, doi:10.3103/S0147687410020067, 2010.

Godwin, C. M., McNamara, P. J. and Markfort, C. D.: Evening methane emission pulses from a boreal wetland correspond to convective mixing in hollows, J. Geophys. Res. Biogeosciences, 118(3), 994–1005, doi:10.1002/jgrg.20082, 2013.

Griffin, D. M.: Water potential as a selective factor in the microbial ecology of soils, in Water Potential Relations in Soil Microbiology edited by: Parr, J., Gardner,W., and Elliott, L., pp. 141–151, Soil Sci. Soc. Am., 1981.

Houweling, S., Bergamaschi, P., Chevallier, F., Heimann, M., Kaminski, T., Krol, M., Michalak, A. M. and Patra, P.: Global inverse modeling of CH4 sources and sinks: an overview of methods, Atmos Chem Phys, 17(1), 235–256, doi:10.5194/acp-17-235-2017, 2017.

Hurtt, G. C., Frolking, S., Fearon, M. G., Moore, B., Shevliakova, E., Malyshev, S., Pacala, S. W. and Houghton, R. A.: The underpinnings of land-use history: three centuries of global gridded land-use transitions, wood-harvest activity, and resulting secondary lands, Glob. Change Biol., 12(7), 1208–1229, doi:10.1111/j.1365-2486.2006.01150.x, 2006.

Jones, C., Robertson, E., Arora, V., Friedlingstein, P., Shevliakova, E., Bopp, L., Brovkin, V., Hajima, T., Kato, E., Kawamiya, M., Liddicoat, S., Lindsay, K., Reick, C. H., Roelandt, C., Segschneider, J. and Tjiputra, J.: Twenty-First-Century Compatible CO2 Emissions and

1208 Airborne Fraction Simulated by CMIP5 Earth System Models under Four Representative
1209 Concentration Pathways, J. Clim., 26(13), 4398–4413, doi:10.1175/JCLI-D-12-00554.1,
1210 2013.

1211 Kaplan, J. O.: Wetlands at the Last Glacial Maximum: Distribution and methane emissions,
1212 Geophys. Res. Lett., 29(6), 3–1, doi:10.1029/2001GL013366, 2002.

1213 Kim, H.-S., Maksyutov, S., Glagolev, M. V., Machida, T., Patra, P. K., Sudo, K. and Inoue,
1214 G.: Evaluation of methane emissions from West Siberian wetlands based on inverse
1215 modeling, Environ. Res. Lett., 6(3), 035201, 2011.

1216 Kloster, S., Mahowald, N. M., Randerson, J. T., Thornton, P. E., Hoffman, F. M., Levis, S.,
1217 Lawrence, P. J., Feddema, J. J., Oleson, K. W. and Lawrence, D. M.: Fire dynamics during
1218 the 20th century simulated by the Community Land Model, Biogeosciences, 7(6), 1877–
1219 1902, doi:10.5194/bg-7-1877-2010, 2010.

1220 Lamarque, J.-F., Bond, T. C., Eyring, V., Granier, C., Heil, A., Klimont, Z., Lee, D., Liousse,
1221 C., Mieville, A., Owen, B., Schultz, M. G., Shindell, D., Smith, S. J., Stehfest, E., Van
1222 Aardenne, J., Cooper, O. R., Kainuma, M., Mahowald, N., McConnell, J. R., Naik, V., Riahi,
1223 K. and van Vuuren, D. P.: Historical (1850–2000) gridded anthropogenic and biomass
1224 burning emissions of reactive gases and aerosols: methodology and application,
1225 Atmospheric Chem. Phys., 10(15), 7017–7039, doi:10.5194/acp-10-7017-2010, 2010.

1226 Lamarque, J.-F., Shindell, D. T., Josse, B., Young, P. J., Cionni, I., Eyring, V., Bergmann, D.,
1227 Cameron-Smith, P., Collins, W. J., Doherty, R., Dalsoren, S., Faluvegi, G., Folberth, G.,
1228 Ghan, S. J., Horowitz, L. W., Lee, Y. H., MacKenzie, I. A., Nagashima, T., Naik, V.,
1229 Plummer, D., Righi, M., Rumbold, S. T., Schulz, M., Skeie, R. B., Stevenson, D. S., Strode,
1230 S., Sudo, K., Szopa, S., Voulgarakis, A. and Zeng, G.: The Atmospheric Chemistry and
1231 Climate Model Intercomparison Project (ACCMIP): overview and description of models,
1232 simulations and climate diagnostics, Geosci. Model Dev., 6(1), 179–206, doi:10.5194/gmd-6-
1233 179-2013, 2013.

1234 Langer, M., Westermann, S., Walter Anthony, K., Wischnewski, K. and Boike, J.: Frozen
1235 ponds: production and storage of methane during the Arctic winter in a lowland tundra
1236 landscape in northern Siberia, Lena River delta, Biogeosciences, 12(4), 977–990,
1237 doi:10.5194/bg-12-977-2015, 2015.

1238 Le Quéré, C., Andrew, R. M., Friedlingstein, P., Sitch, S., Pongratz, J., Manning, A. C.,
1239 Korsbakken, J. I., Peters, G. P., Canadell, J. G., Jackson, R. B., Boden, T. A., Tans, P. P.,
1240 Andrews, O. D., Arora, V. K., Bakker, D. C. E., Barbero, L., Becker, M., Betts, R. A., Bopp,
1241 L., Chevallier, F., Chini, L. P., Ciais, P., Cosca, C. E., Cross, J., Currie, K., Gasser, T.,
1242 Harris, I., Hauck, J., Haverd, V., Houghton, R. A., Hunt, C. W., Hurtt, G., Ilyina, T., Jain, A.
1243 K., Kato, E., Kautz, M., Keeling, R. F., Klein Goldewijk, K., Körtzinger, A., Landschützer, P.,
1244 Lefèvre, N., Lenton, A., Lienert, S., Lima, I., Lombardozzi, D., Metzl, N., Millero, F., Monteiro,
1245 P. M. S., Munro, D. R., Nabel, J. E. M. S., Nakaoka, S.-I., Nojiri, Y., Padin, X. A., Peregon,
1246 A., Pfeil, B., Pierrot, D., Poulter, B., Rehder, G., Reimer, J., Rödenbeck, C., Schwinger, J.,
1247 Séférian, R., Skjelvan, I., Stocker, B. D., Tian, H., Tilbrook, B., Tubiello, F. N., van der Laan-
1248 Luijkx, I. T., van der Werf, G. R., van Heuven, S., Viovy, N., Vuichard, N., Walker, A. P.,
1249 Watson, A. J., Wiltshire, A. J., Zaehle, S. and Zhu, D.: Global Carbon Budget 2017, Earth
1250 Syst. Sci. Data, 10(1), 405–448, doi:10.5194/essd-10-405-2018, 2018.

1251 Lehner, B. and Döll, P.: Development and validation of a global database of lakes, reservoirs
1252 and wetlands, J. Hydrol., 296(1–4), 1–22, doi:10.1016/j.jhydrol.2004.03.028, 2004.

Li, F., Zeng, X. D. and Levis, S.: A process-based fire parameterization of intermediate complexity in a Dynamic Global Vegetation Model, Biogeosciences Discuss., 9(3), 3233–3287, doi:10.5194/bgd-9-3233-2012, 2012.

Marlon, J. R., Bartlein, P. J., Carcaillet, C., Gavin, D. G., Harrison, S. P., Higuera, P. E., Joos, F., Power, M. J. and Prentice, I. C.: Climate and human influences on global biomass burning over the past two millennia, Nat. Geosci, 1(10), 697–702, doi:10.1038/ngeo313, 2008.

Matthes, K., Funke, B., Andersson, M. E., Barnard, L., Beer, J., Charbonneau, P., Clilverd, M. A., Dudok de Wit, T., Haberreiter, M., Hendry, A., Jackman, C. H., Kretzschmar, M., Kruschke, T., Kunze, M., Langematz, U., Marsh, D. R., Maycock, A. C., Misios, S., Rodger, C. J., Scaife, A. A., Seppälä, A., Shangguan, M., Sinnhuber, M., Tourpali, K., Usoskin, I., van de Kamp, M., Verronen, P. T. and Versick, S.: Solar forcing for CMIP6 (v3.2), Geosci. Model Dev., 10(6), 2247–2302, doi:10.5194/gmd-10-2247-2017, 2017.

Matthews, E. and Fung, I.: Methane emission from natural wetlands: Global distribution, area, and environmental characteristics of sources, Glob. Biogeochem. Cycles, 1(1), 61–86, doi:10.1029/GB001i001p00061, 1987.

Meinshausen, M., Smith, S. J., Calvin, K., Daniel, J. S., Kainuma, M. L. T., Lamarque, J.-F., Matsumoto, K., Montzka, S. A., Raper, S. C. B., Riahi, K., Thomson, A., Velders, G. J. M. and van Vuuren, D. P. P.: The RCP greenhouse gas concentrations and their extensions from 1765 to 2300, Clim. Change, 109(1), 213, doi:10.1007/s10584-011-0156-z, 2011.

Melton, J. R. and Arora, V. K.: Sub-grid scale representation of vegetation in global land surface schemes: implications for estimation of the terrestrial carbon sink, Biogeosciences, 11(4), 1021–1036, doi:10.5194/bg-11-1021-2014, 2014.

Melton, J. R. and Arora, V. K.: Competition between plant functional types in the Canadian Terrestrial Ecosystem Model (CTEM) v. 2.0, Geosci Model Dev, 9(1), 323–361, doi:10.5194/gmd-9-323-2016, 2016.

Melton, J. R., Wania, R., Hodson, E. L., Poulter, B., Ringeval, B., Spahni, R., Bohn, T., Avis, C. A., Beerling, D. J., Chen, G., Eliseev, A. V., Denisov, S. N., Hopcroft, P. O., Lettenmaier, D. P., Riley, W. J., Singarayer, J. S., Subin, Z. M., Tian, H., Zürcher, S., Brovkin, V., van Bodegom, P. M., Kleinen, T., Yu, Z. C. and Kaplan, J. O.: Present state of global wetland extent and wetland methane modelling: conclusions from a model inter-comparison project (WETCHIMP), Biogeosciences, 10(2), 753–788, doi:10.5194/bg-10-753-2013, 2013.

Melton, J. R., Shrestha, R. K. and Arora, V. K.: The influence of soils on heterotrophic respiration exerts a strong control on net ecosystem productivity in seasonally dry Amazonian forests, Biogeosciences, 12(4), 1151–1168, doi:10.5194/bg-12-1151-2015, 2015.

Migliavacca, M., Dosio, A., Kloster, S., Ward, D. S., Camia, A., Houborg, R., Houston Durrant, T., Khabarov, N., Krasovskii, A. A., San Miguel-Ayanz, J. and Cescatti, A.: Modeling burned area in Europe with the Community Land Model, J. Geophys. Res. Biogeosciences, 118(1), 265–279, doi:10.1002/jgrg.20026, 2013.

Myhre, G., Shindell, D., Bréon, F.-M., Collins, W., Fuglestvedt, J., Huang, J., Koch, D., Lamarque, J.-F., Lee, D., Mendoza, B., Nakajima, T., Robock, A., Stephens, G., Takemura, T. and Zhang, H.: Anthropogenic and Natural Radiative Forcing, in Climate Change 2013: The Physical Science Basis. Contribution of Working Group I to the Fifth Assessment Report of the Intergovernmental Panel on Climate Change, edited by T. F. Stocker, D. Qin, G.-K.

1298 Plattner, M. Tignor, S. K. Allen, J. Boschung, A. Nauels, Y. Xia, V. Bex, and P. M. Midgley,
1299 pp. 659–740, Cambridge University Press, Cambridge, United Kingdom and New York, NY,
1300 USA., 2013.

1301 Naik, V., Voulgarakis, A., Fiore, A. M., Horowitz, L. W., Lamarque, J.-F., Lin, M., Prather, M.
1302 J., Young, P. J., Bergmann, D., Cameron-Smith, P. J., Cionni, I., Collins, W. J., Dalsøren, S.
1303 B., Doherty, R., Eyring, V., Faluvegi, G., Folberth, G. A., Josse, B., Lee, Y. H., MacKenzie, I.
1304 A., Nagashima, T., van Noije, T. P. C., Plummer, D. A., Righi, M., Rumbold, S. T., Skeie, R.,
1305 Shindell, D. T., Stevenson, D. S., Strode, S., Sudo, K., Szopa, S. and Zeng, G.: Preindustrial
1306 to present-day changes in tropospheric hydroxyl radical and methane lifetime from the
1307 Atmospheric Chemistry and Climate Model Intercomparison Project (ACCMIP), Atmospheric
1308 Chem. Phys., 13(10), 5277–5298, doi:10.5194/acp-13-5277-2013, 2013.

1309 Neely III, R. R., Conley, A. J., Vitt, F. and Lamarque, J.-F.: A consistent prescription of
1310 stratospheric aerosol for both radiation and chemistry in the Community Earth System Model
1311 (CESM1), Geosci. Model Dev., 9(7), 2459–2470, doi:10.5194/gmd-9-2459-2016, 2016.

1312 Papa, F., Prigent, C., Aires, F., Jimenez, C., Rossow, W. B. and Matthews, E.: Interannual
1313 variability of surface water extent at the global scale, 1993–2004, J. Geophys. Res.
1314 Atmospheres, 115(D12), n/a-n/a, doi:10.1029/2009JD012674, 2010.

1315 Peng, Y., Arora, V. K., Kurz, W. A., Hember, R. A., Hawkins, B. J., Fyfe, J. C. and Werner,
1316 A. T.: Climate and atmospheric drivers of historical terrestrial carbon uptake in the province
1317 of British Columbia, Canada, Biogeosciences, 11(3), 635–649, doi:10.5194/bg-11-635-2014,
1318 2014.

1319 Peregon, A., Maksyutov, S. and Yamagata, Y.: An image-based inventory of the spatial
1320 structure of West Siberian wetlands, Environ. Res. Lett., 4(4), 045014, 2009.

1321 Poulter, B., Bousquet, P., Canadell, J. G., Ciais, P., Peregon, A., Marielle Saunois, Arora, V.
1322 K., Beerling, D. J., Brovkin, V., Jones, C. D., Joos, F., Nicola Gedney, Ito, A., Kleinen, T.,
1323 Koven, C. D., McDonald, K., Melton, J. R., Peng, C., Shushi Peng, Prigent, C., Schroeder,
1324 R., Riley, W. J., Saito, M., Spahni, R., Tian, H., Lyla Taylor, Viovy, N., Wilton, D., Wiltshire,
1325 A., Xu, X., Zhang, B., Zhang, Z. and Zhu, Q.: Global wetland contribution to 2000–2012
1326 atmospheric methane growth rate dynamics, Environ. Res. Lett., 12(9), 094013, 2017.

1327 Prather, M. J., Holmes, C. D. and Hsu, J.: Reactive greenhouse gas scenarios: Systematic
1328 exploration of uncertainties and the role of atmospheric chemistry, Geophys. Res. Lett.,
1329 39(9), n/a-n/a, doi:10.1029/2012GL051440, 2012.

1330 Prigent, C., Papa, F., Aires, F., Rossow, W. B. and Matthews, E.: Global inundation
1331 dynamics inferred from multiple satellite observations, 1993–2000, J. Geophys. Res.
1332 Atmospheres, 112(D12), n/a-n/a, doi:10.1029/2006JD007847, 2007.

1333 Randerson, J. T., Chen, Y., van der Werf, G. R., Rogers, B. M. and Morton, D. C.: Global
1334 burned area and biomass burning emissions from small fires, J. Geophys. Res.
1335 Biogeosciences, 117(G4), n/a-n/a, doi:10.1029/2012JG002128, 2012.

1336 Saunois, M., Bousquet, P., Poulter, B., Peregon, A., Ciais, P., Canadell, J. G., Dlugokencky,
1337 E. J., Etiope, G., Bastviken, D., Houweling, S., Janssens-Maenhout, G., Tubiello, F. N.,
1338 Castaldi, S., Jackson, R. B., Alexe, M., Arora, V. K., Beerling, D. J., Bergamaschi, P., Blake,
1339 D. R., Brailsford, G., Brovkin, V., Bruhwiler, L., Crevoisier, C., Crill, P., Covey, K., Curry, C.,
1340 Frankenberg, C., Gedney, N., Höglund-Isaksson, L., Ishizawa, M., Ito, A., Joos, F., Kim, H.-
1341 S., Kleinen, T., Krummel, P., Lamarque, J.-F., Langenfelds, R., Locatelli, R., Machida, T.,
1342 Maksyutov, S., McDonald, K. C., Marshall, J., Melton, J. R., Morino, I., Naik, V., O'Doherty,

1343   S., Parmentier, F.-J. W., Patra, P. K., Peng, C., Peng, S., Peters, G. P., Pison, I., Prigent, C.,
1344   Prinn, R., Ramonet, M., Riley, W. J., Saito, M., Santini, M., Schroeder, R., Simpson, I. J.,
1345   Spahni, R., Steele, P., Takizawa, A., Thornton, B. F., Tian, H., Tohjima, Y., Viovy, N.,
1346   Voulgarakis, A., van Weele, M., van der Werf, G. R., Weiss, R., Wiedinmyer, C., Wilton, D.
1347   J., Wiltshire, A., Worthy, D., Wunch, D., Xu, X., Yoshida, Y., Zhang, B., Zhang, Z. and Zhu,
1348   Q.: The global methane budget 2000–2012, Earth Syst Sci Data, 8(2), 697–751,
1349   doi:10.5194/essd-8-697-2016, 2016.

1350   Schroeder, R., McDonald, C. K., Chapman, D. B., Jensen, K., Podest, E., Tessler, D. Z.,
1351   Bohn, J. T. and Zimmermann, R.: Development and Evaluation of a Multi-Year Fractional
1352   Surface Water Data Set Derived from Active/Passive Microwave Remote Sensing Data,
1353   Remote Sens., 7(12), doi:10.3390/rs71215843, 2015.

1354   Scinocca, J. F., McFarlane, N. A., Lazare, M., Li, J. and Plummer, D.: Technical Note: The
1355   CCCma third generation AGCM and its extension into the middle atmosphere, Atmospheric
1356   Chem. Phys., 8(23), 7055–7074, doi:10.5194/acp-8-7055-2008, 2008.

1357   Shindell, D., Kuylenstierna, J. C. I., Vignati, E., van Dingenen, R., Amann, M., Klimont, Z.,
1358   Anenberg, S. C., Muller, N., Janssens-Maenhout, G., Raes, F., Schwartz, J., Faluvegi, G.,
1359   Pozzoli, L., Kupiainen, K., Höglund-Isaksson, L., Emberson, L., Streets, D., Ramanathan, V.,
1360   Hicks, K., Oanh, N. T. K., Milly, G., Williams, M., Demkine, V. and Fowler, D.:
1361   Simultaneously Mitigating Near-Term Climate Change and Improving Human Health and
1362   Food Security, Science, 335(6065), 183–189, 2012.

1363   Shindell, D. T., Pechony, O., Voulgarakis, A., Faluvegi, G., Nazarenko, L., Lamarque, J.-F.,
1364   Bowman, K., Milly, G., Kovari, B., Ruedy, R. and Schmidt, G. A.: Interactive ozone and
1365   methane chemistry in GISS-E2 historical and future climate simulations, Atmos Chem Phys,
1366   13(5), 2653–2689, doi:10.5194/acp-13-2653-2013, 2013.

1367   SPARC CCMVal: SPARC Report on the Evaluation of Chemistry-Climate Models, V. Eyring,
1368   T. G. Shepherd, D. W. Waugh (Eds.), SPARC Report No. 5, WCRP-132, WMO/TD-No.
1369   1526., 2010.

1370   Thornton Brett, F., Wik, M. and Carill Patrick, M.: Double-counting challenges the accuracy
1371   of high-latitude methane inventories, Geophys. Res. Lett., 43(24), 12,569-12,577,
1372   doi:10.1002/2016GL071772, 2016.

1373   Verseghy, D. L.: Class—A Canadian land surface scheme for GCMS. I. Soil model, Int. J.
1374   Climatol., 11(2), 111–133, doi:10.1002/joc.3370110202, 1991.

1375   Verseghy, D. L.: The Canadian land surface scheme (CLASS): Its history and future,
1376   Atmosphere-Ocean, 38(1), 1–13, doi:10.1080/07055900.2000.9649637, 2000.

1377   Verseghy, D. L., McFarlane, N. A. and Lazare, M.: Class—A Canadian land surface scheme
1378   for GCMS, II. Vegetation model and coupled runs, Int. J. Climatol., 13(4), 347–370,
1379   doi:10.1002/joc.3370130402, 1993.

1380   Viovy, N.: CRU-NCEP reanalysis data version 4, [online] Available from:
1381   http://dods.extra.cea.fr/store/p529viov/cruncep/V4_1901_2012/, 2012.

1382   Voulgarakis, A., Naik, V., Lamarque, J.-F., Shindell, D. T., Young, P. J., Prather, M. J., Wild,
1383   O., Field, R. D., Bergmann, D., Cameron-Smith, P., Cionni, I., Collins, W. J., Dalsøren, S. B.,
1384   Doherty, R. M., Eyring, V., Faluvegi, G., Folberth, G. A., Horowitz, L. W., Josse, B.,
1385   MacKenzie, I. A., Nagashima, T., Plummer, D. A., Righi, M., Rumbold, S. T., Stevenson, D.
1386   S., Strode, S. A., Sudo, K., Szopa, S. and Zeng, G.: Analysis of present day and future OH

1387 and methane lifetime in the ACCMIP simulations, Atmos Chem Phys, 13(5), 2563–2587,
1388 doi:10.5194/acp-13-2563-2013, 2013.

1389 Walter, B. P. and Heimann, M.: A process-based, climate-sensitive model to derive methane
1390 emissions from natural wetlands: Application to five wetland sites, sensitivity to model
1391 parameters, and climate, Glob. Biogeochem. Cycles, 14(3), 745–765,
1392 doi:10.1029/1999GB001204, 2000.

1393 Wania, R., Ross, I. and Prentice, I. C.: Implementation and evaluation of a new methane
1394 model within a dynamic global vegetation model: LPJ-WHyMe v1.3.1, Geosci Model Dev,
1395 3(2), 565–584, doi:10.5194/gmd-3-565-2010, 2010.

1396 Winderlich, J.: Setup of a CO2 and CH4 measurement system in Central Siberia and
1397 modeling of its results, Max-Planck-Institut für Biogeochemie, Jena. [online] Available from:
1398 http://ediss.sub.uni-hamburg.de/volltexte/2012/5533/pdf/Dissertation.pd, 2012.

1399 Young, P. J., Archibald, A. T., Bowman, K. W., Lamarque, J.-F., Naik, V., Stevenson, D. S.,
1400 Tilmes, S., Voulgarakis, A., Wild, O., Bergmann, D., Cameron-Smith, P., Cionni, I., Collins,
1401 W. J., Dalsøren, S. B., Doherty, R. M., Eyring, V., Faluvegi, G., Horowitz, L. W., Josse, B.,
1402 Lee, Y. H., MacKenzie, I. A., Nagashima, T., Plummer, D. A., Righi, M., Rumbold, S. T.,
1403 Skeie, R. B., Shindell, D. T., Strode, S. A., Sudo, K., Szopa, S. and Zeng, G.: Pre-industrial
1404 to end 21st century projections of tropospheric ozone from the Atmospheric Chemistry and
1405 Climate Model Intercomparison Project (ACCMIP), Atmospheric Chem. Phys., 13(4), 2063–
1406 2090, doi:10.5194/acp-13-2063-2013, 2013.

1407 Zhu, Q., Liu, J., Peng, C., Chen, H., Fang, X., Jiang, H., Yang, G., Zhu, D., Wang, W. and
1408 Zhou, X.: Modelling methane emissions from natural wetlands by development and
1409 application of the TRIPLEX-GHG model, Geosci Model Dev, 7(3), 981–999,
1410 doi:10.5194/gmd-7-981-2014, 2014a.

1411 Zhu, X., Zhuang, Q., Lu, X. and Song, L.: Spatial scale-dependent land–atmospheric
1412 methane exchanges in the northern high latitudes from 1993 to 2004, Biogeosciences, 11(7),
1413 1693–1704, doi:10.5194/bg-11-1693-2014, 2014b.

1414 Zobler, L.: A World Soil File for Global Climate Modelling, NASA Technical Memorandum
1415 87802, NASA Goddard Institute for Space Studies, New York, USA., 1986.

1416 Zona, D., Gioli, B., Commane, R., Lindaas, J., Wofsy, S. C., Miller, C. E., Dinardo, S. J.,
1417 Dengel, S., Sweeney, C., Karion, A., Chang, R. Y.-W., Henderson, J. M., Murphy, P. C.,
1418 Goodrich, J. P., Moreaux, V., Liljedahl, A., Watts, J. D., Kimball, J. S., Lipson, D. A. and
1419 Oechel, W. C.: Cold season emissions dominate the Arctic tundra methane budget, Proc.
1420 Natl. Acad. Sci., 113(1), 40–45, 2016.

1421

1422

1423

1424

1425

1426 **Table** 1: Emissions categories for EDGAR and RCP anthropogenic methane emissions.

1427

EDGAR	RCP
Non-biomass burning categories	
1. Energy manufacturing transformation 2. Non-road transportation 3. Road transportation 4. Residential 5. Fugitive from solid 6. Oil production and refineries 7. Gas production and distribution 8. Industrial processes and product use 9. Enteric fermentation 10. Manure management 11. Agricultural soils 12. Agricultural waste burning 13. Soil waste disposal 14. Waste waster 15. Fossil fuel fires	1. Agricultural sector 2. Agricultural waste burning 3. Residential and commercial combustion 4. Energy production and distribution 5. Industrial processes and combustion 6. Land transport emissions 7. Waste treatment and disposal 8. Shipping
Biomass burning categories	
16. Large scale biomass burning	9. Biomass burning from forest fires 10. Biomass burning from grass fires

1428

1429

1430 **Table** 2: Comparison of CLASS-CTEM simulated annual methane emissions and annual
1431 maximum wetland extent for the West Siberia lowlands (WSL) region with models
1432 participating in the WETCHIMP-WSL intercomparison and observation- and inversion-based
1433 estimates as discussed in section 3.5. Numbers shown are mean ± standard error from Bohn
1434 et al. (2015) for models participating in the WETCHIMP-WSL intercomparison. Standard
1435 error is not available for all inversions. All values are reported as average for the period
1436 1993-2004 unless otherwise noted.

1437

WSL annual maximum wetland extent (million km^2)	
Model mean from participating models in the WETCHIMP-WSL Intercomparison	0.70±0.15
CLASS-CTEM (this study)	0.53
GIEMS inundation data set	0.21
SWAMPS inundation data set	0.15
SWAMPS and GCP product (for period 2002-2012)	0.55
Peregon et al. (2009)	0.68
WSL annual wetland emissions (Tg CH$_4$/yr)	
Model mean from participating models in the WETCHIMP-WSL Intercomparison	5.34±0.54
CLASS-CTEM (this study)	7.76
Bousquet 2011 K	7.06
Bousquet 2011 R	7.13
Kim 2011 (for year 2005)	3.08±1.40
Winderlich 2012 (for year 2009)	9.80

1438
1439
1440

1441

1442 Table 3: Comparison of the components of the present day methane budget based on this

1443 study with those from Saunois et al. (2016) (based on synthesis of published studies). The

1444 values used in this study are averaged for the period 2000-2008 (since the last year of the

1445 version of EDGAR emissions used is 2008) while Saunois et al. (2016) values correspond to

1446 the 2000-2009 period.

1447

1448

	Saunois et al. (2016) estimates based on top-down approaches	Values used in this study …	… and how they were obtained.
Natural sources	234 [194-292]	199	
Natural wetlands	166 [125-204]	169	CLASS-CTEM simulated
Other natural sources (termites, geological, fresh water etc.)	68 [21-130]	30	Specified as a constant over the historical period
Anthropogenic sources	319 [255-357]	344	
Agriculture and waste	183 [112-241]	200	EDGAR
Fossil fuels	101 [77-126]	117	EDGAR
Biomass and biofuel burning	35 [16-53]	27	CLASS-CTEM simulated
Sum of all sources	552 [535-566]	543	
Sum of all sinks	546	538	
Atmospheric sink	514	509	Based on specified bias-corrected atmospheric CH4 lifetimes from CMAM
Soil sink	32 [27-38]	29	CLASS-CTEM simulated

1449

1450

1451

1452

1453

1454

1455

1456

1457

1458

1459
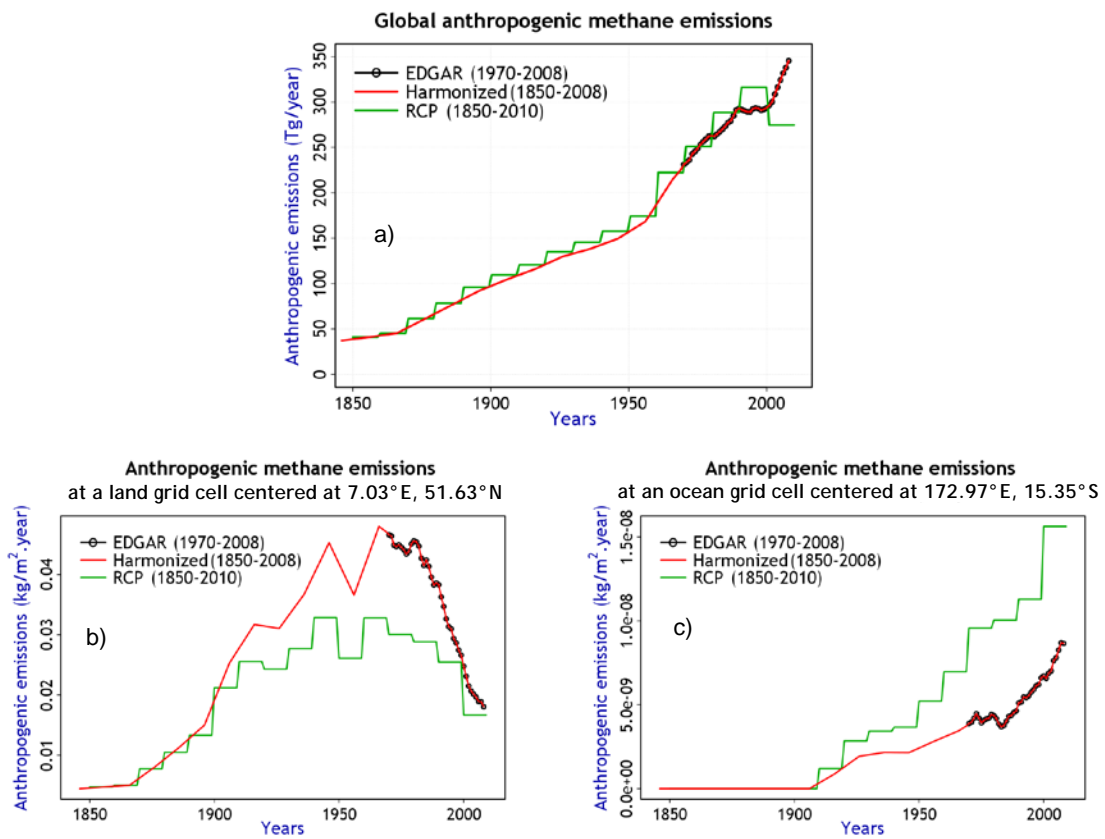
1460

1461 Figure 1: Comparison of RCP, EDGAR and their harmonized annual global anthropogenic
1462 methane emissions (panel a) excluding biomass burning. Panels (b) and (c) illustrate the
1463 harmonization technique for a land and an ocean grid cell, respectively.

1464

1465

1466

1467

1468
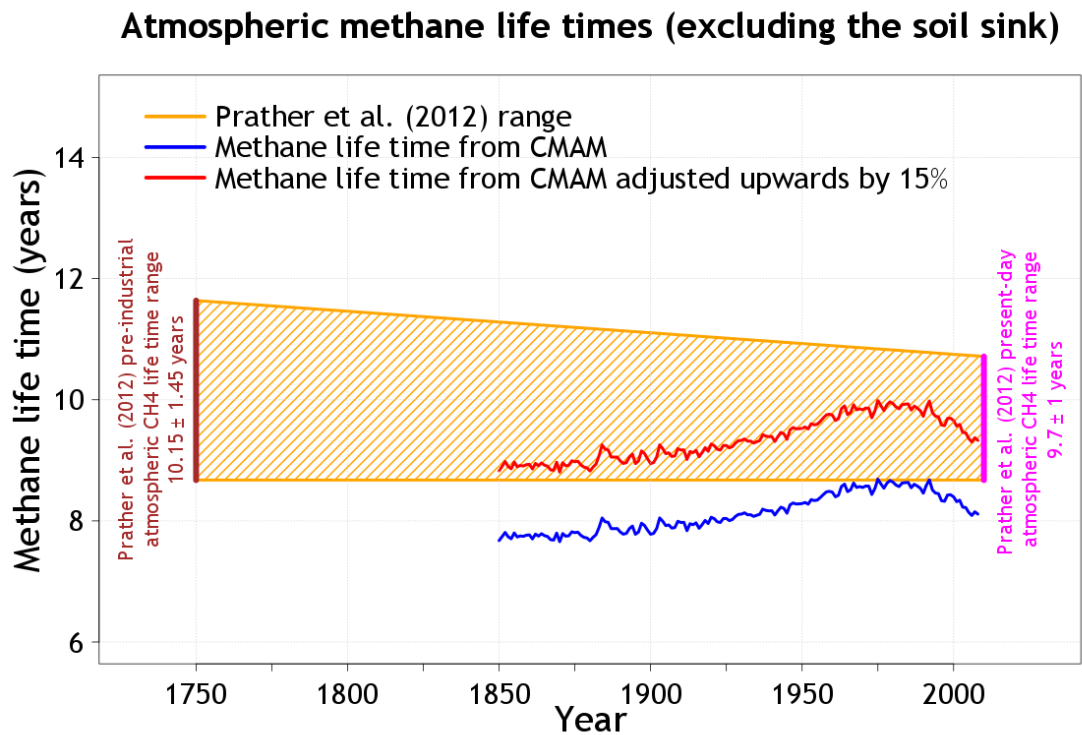
1469

1470 Figure 2: Comparison of atmospheric methane lifetime obtained from the Canadian Middle
1471 Atmosphere Model (CMAM) for the period 1850-2010 with observation-based estimates
1472 from Prather et al. (2012) but excluding the soil sink as explained in section 2.2.3.

1473

1474

1475

1476

CLASS-CTEM simulated natural methane sinks and sources and annual maximum wetland extent
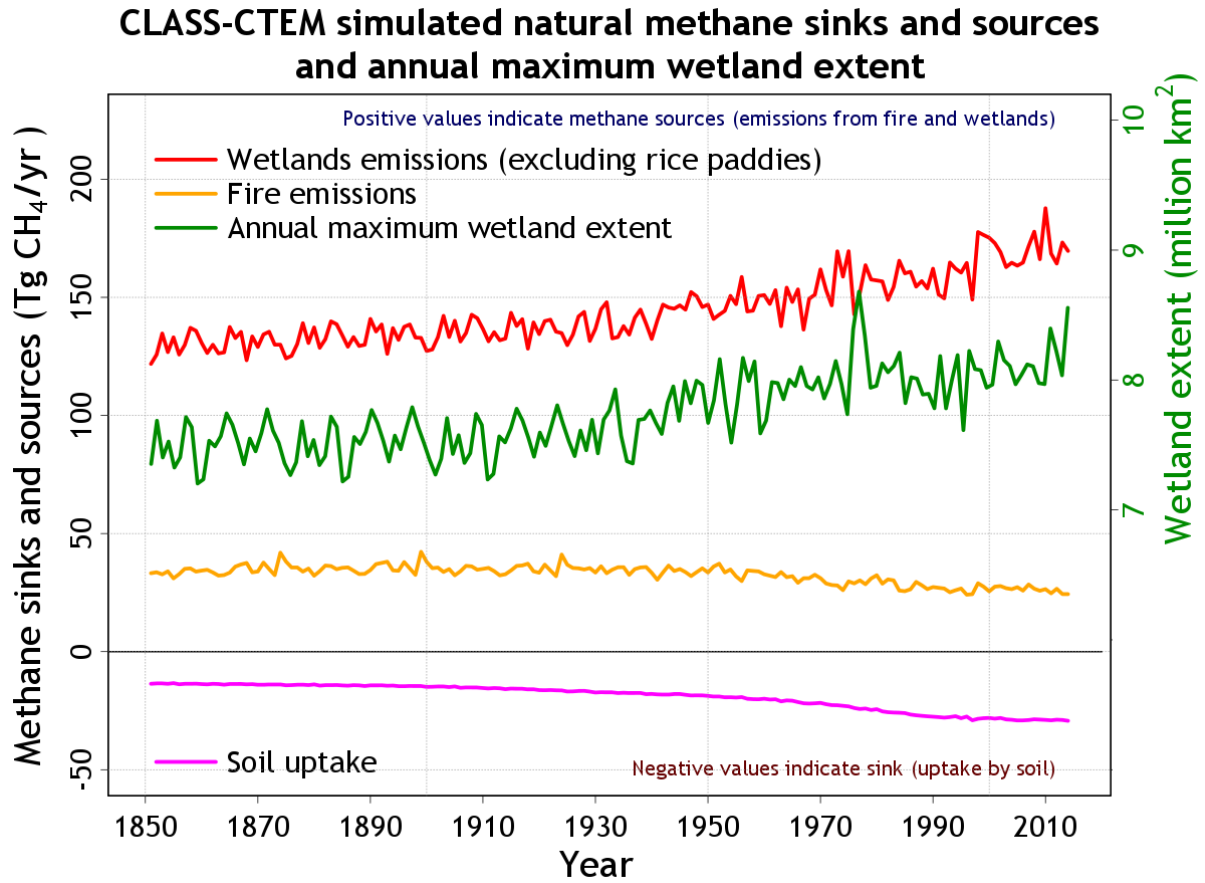
1477

Figure 3: Time evolution of simulated natural methane fluxes (shown on the primary y-axis) and annual maximum wetland extent (shown on the secondary y-axis) by CLASS-CTEM for the 1851-2015 period in the transient historical simulation.

1481

1482

1483

1484
1485 Figure 4: Comparison of simulated methane concentration over the historical period with its
1486 observation-based estimates (panel a). The simulation may be initialized from the 1850
1487 observed methane concentration (solid green line) or from an 1850 concentration that is in
1488 equilibrium with 1850 specified methane sources and sinks (dashed blueline) as explained in
1489 section 3.2. Panel (b) compares the methane lifetimes required to achieve the observed
1490 increase in methane concentration over the historical period (black line) to within ± 3 ppb
1491 (shaded area between grey lines) with observation-based estimate of atmospheric methane
1492 lifetime based on Prather et al. (2012) and the adjusted atmospheric methane lifetime from
1493 CMAM.
1494

1495

1496 Figure 5: Time evolution of simulated natural methane fluxes (shown on the primary y-axis)
1497 and annual maximum wetland extent (shown on the secondary y-axis) by CLASS-CTEM for
1498 the 1851-2008 period for the case when wetland extent and methane emissions are not
1499 allowed to respond to changing climate and increase atmospheric CO_2 over the historical
1500 period (panel a). Panel (b) shows the simulated methane concentration over the historical
1501 period, together with its observation-based values, when the natural fluxes shown in panel (a)
1502 are used within the framework of the one box model of atmospheric methane.

1503

1504

1505
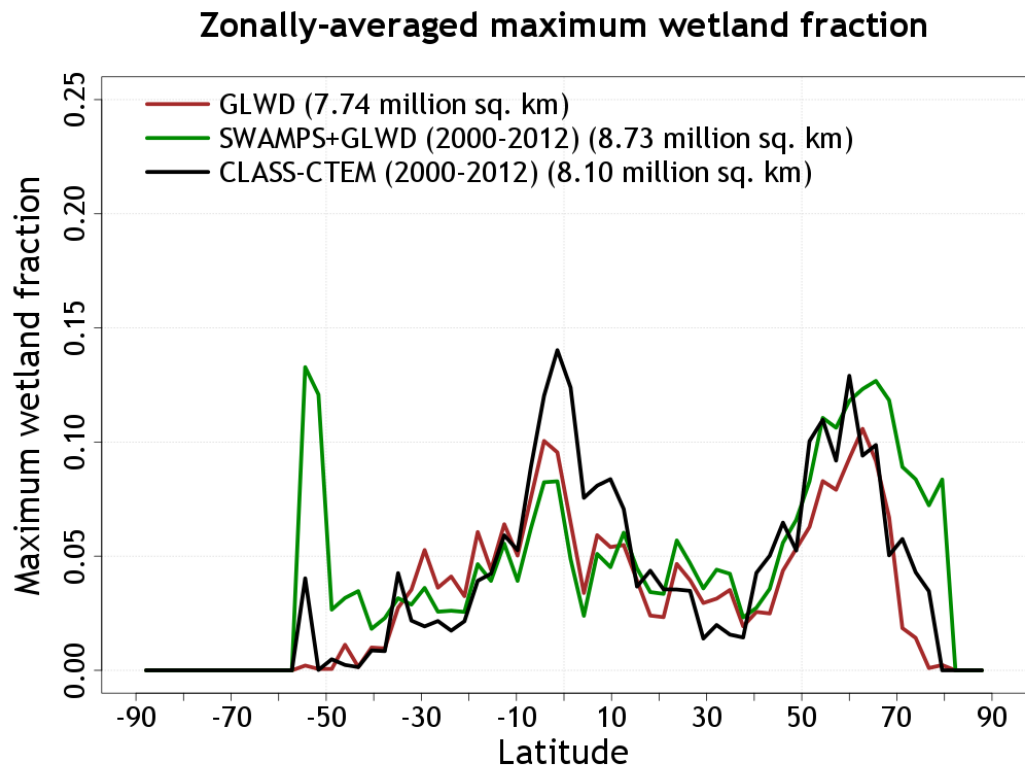
1506

1507 Figure 6: Comparison of simulated zonally-averaged maximum wetland fraction over land
1508 with observation-based estimates based on the Global Lakes and Wetland (GLWD; Lehner
1509 and Döll, 2004) and a new product that is formed by merging remote sensing based
1510 observations of daily surface inundation from the Surface Water Microwave Product Series
1511 (SWAMPS; Schroeder et al., 2015) with the static inventory of wetland area from the GLWD
1512 as explained in Poulter et al. (2017).

1513
1514
1515

1516

1517

1518
1519

1520

1521

1522
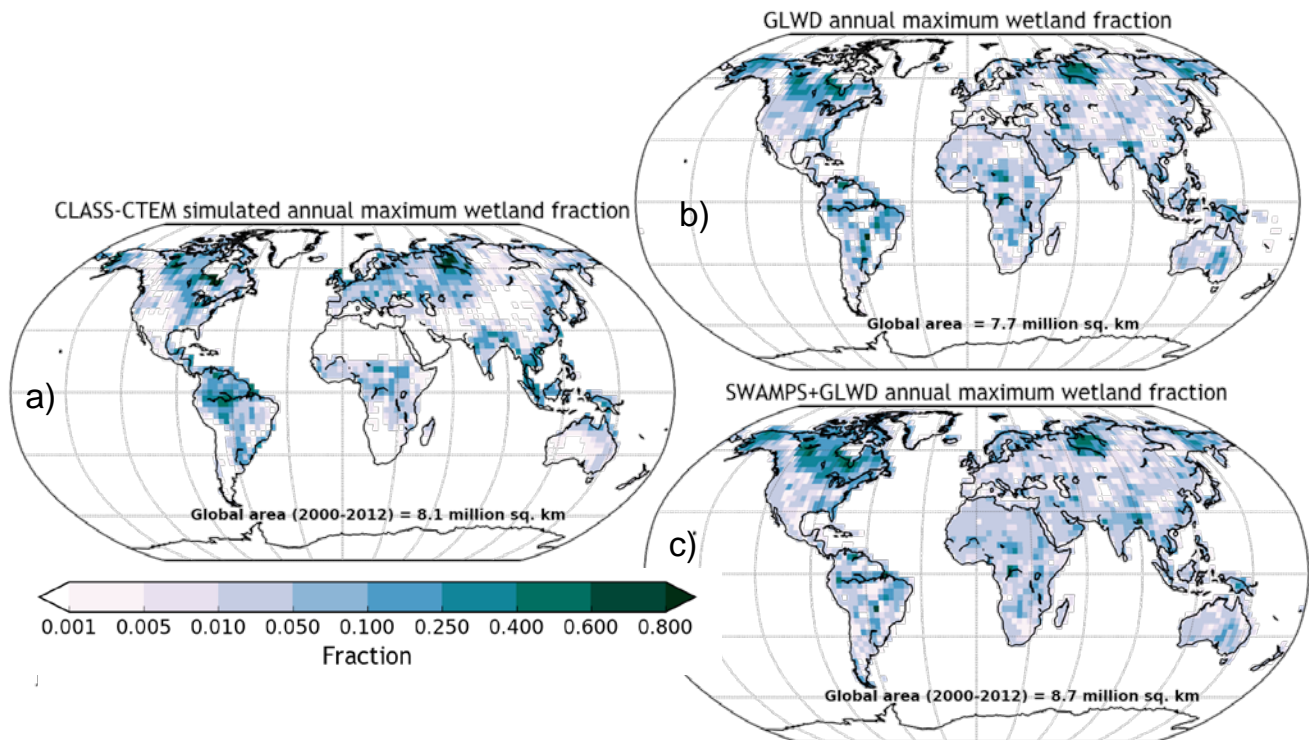
1523   Figure 7: Comparison of geographical distribution simulated annual maximum wetland
1524   fraction with observation-based estimates based on the Global Lakes and Wetland (GLWD;
1525   Lehner and Döll, 2004) and a new product that is formed by merging remote sensing based
1526   observations of daily surface inundation from the Surface Water Microwave Product Series
1527   (SWAMPS; Schroeder et al., 2015) with the static inventory of wetland area from the GLWD
1528   as explained in Poulter et al. (2017).

1529

1530

1531
1532
1533

1534

1535

1536

1537

1538

1539

1540
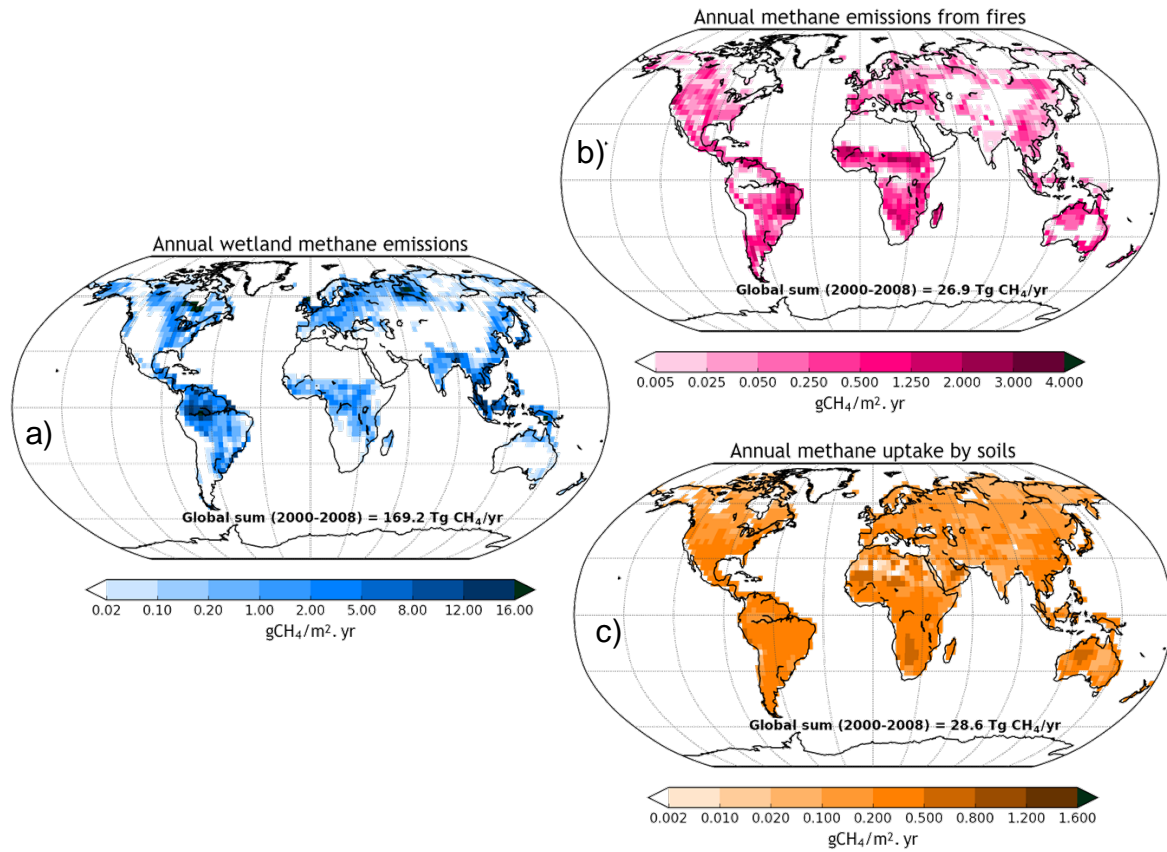
1541

Figure 8: Geographical distribution of annual emissions from wetlands (panel a) and fire (panel c), and the soil sink (panel b) simulated by the CLASS-CTEM model. The data are averaged over the 2000-2009 period.

1545

1546

1547
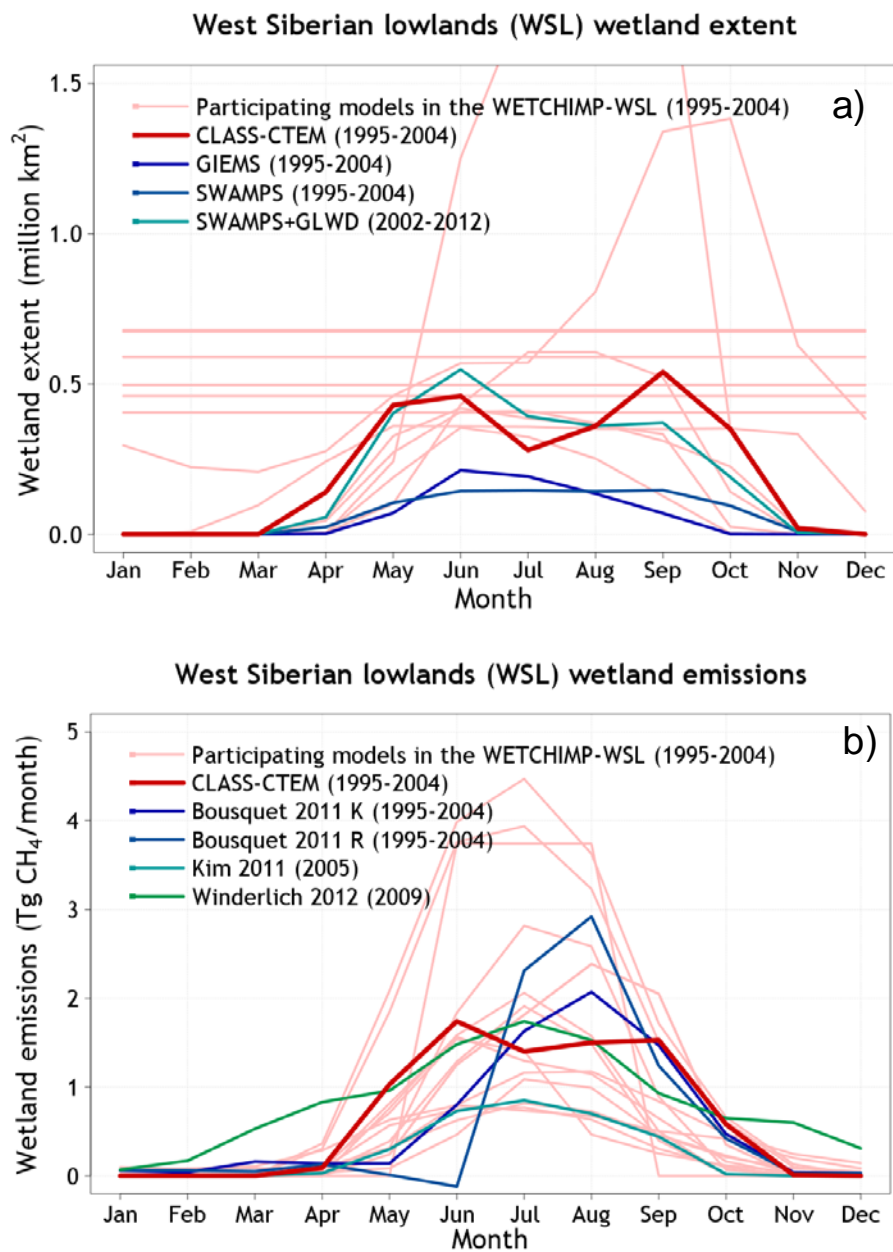
1548

1549 Figure 9: Comparison of CLASS-CTEM simulated wetland extend (panel a) and wetland
1550 methane emissions (pane; b) over the West Siberian lowlands (WSL) region with those from
1551 models participating in the WETCHIMP-WSL intercomparison and observation- and
1552 inversion-based estimates as discussed in section 3.5.

1553

1554

1555

1556

1557

1558

1559
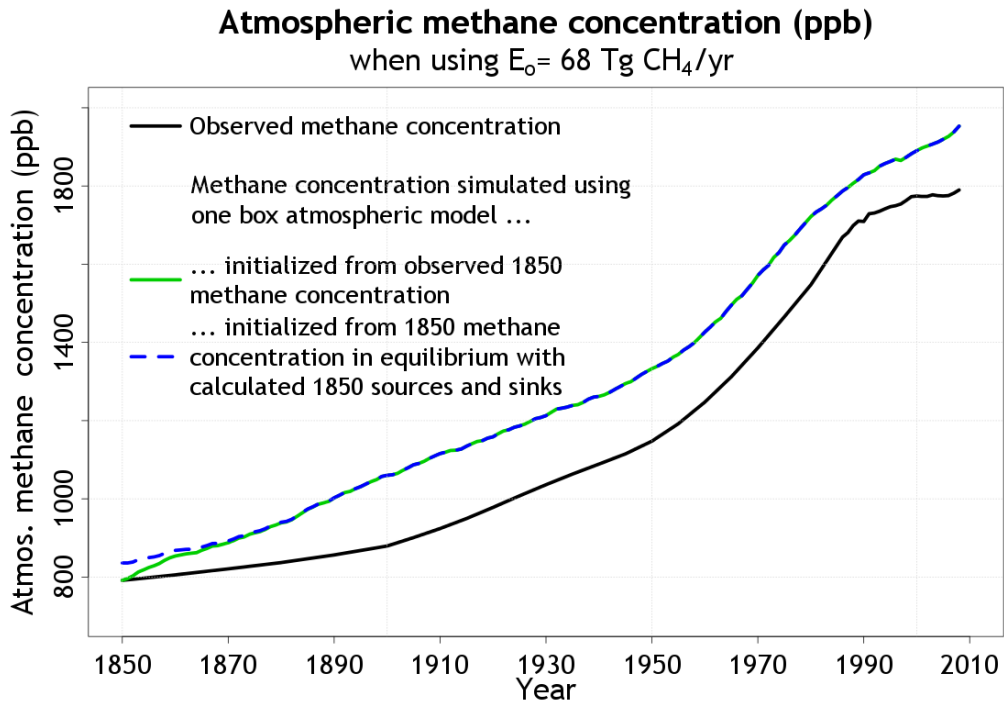
1560

1561   Figure 10: Simulated methane concentration over the historical period, together with its
1562   observation-based values, when other non-wetland natural methane emissions (E_o) are
1563   specified at 68 Tg CH_4/yr over the historical period.

1564

1565

1566 **Appendix A: Calculation of wetland extent**

1567

1568 The distribution of wetlands is based on a simple formulation which takes into account the

1569 topography in a grid cell and its simulated grid-averaged soil moisture content similar to

1570 Kaplan (2002). The ETOPO1 digital elevation data (Amante and Eakins, 2009) are used to

1571 calculate slopes at 1 arc minute (1/60th degree) resolution. Each 1 arc minute grid cell is

1572 assigned a slope that is the average of eight slopes based on its elevation and the elevation of

1573 its eight surrounding grid cells. The objective is to find what fraction of a grid cell, at some

1574 given resolution, has slopes flatter than a given slope threshold. Figure A1 displays the

1575 fraction of each 0.5 degree grid cell with slopes less than the threshold of 0.002 (i.e. 0.2%

1576 slope) calculated using 1 arc minute slopes, hereafter referred to as the "flat" fraction of a

1577 grid cell (f_s). The flat fraction of grid cell is also shown at the current operational 2.81°

1578 resolution of CanESM4.2, which is the spatial resolution we have used in this study. Figure 1

1579 shows that the approach is able to identify the flat regions of the world including the West

1580 Siberian and Hudson Bay lowlands, parts of northern Africa and in South America the

1581 Pantanal and the region bordering Argentina, Paraguay and Uruguay.

1582

1583 The flat fraction is the maximum fraction of a grid cell that can potentially become a wetland,

1584 if soils are sufficiently wet, and thus a source of CH_4 emissions. As the grid-averaged

1585 simulated soil wetness (w) of the top soil layer increases, above a given lower threshold (w_{low})

1586 in a grid cell, its wetland fraction (f_w) is assumed to increase linearly until some specified

1587 higher soil wetness threshold (w_{high}) up to a maximum value equal to the flat fraction (f_s) in a

1588 grid cell.

1589
$$f_w = \max\left(0, \min\left(f_s, \left(\frac{w - w_{low}}{w_{high} - w_{low}}\right) f_s\right)\right) \tag{A1}$$

1590

1591   Soil wetness ($w = \frac{\theta_l}{\theta_p}$) itself is defined as the ratio of volumetric liquid soil moisture content

1592   (θ_l) to the soil porosity (θ_p) for the top soil layer. The remaining fraction of the grid cell

1593   ($1 - f_w$) is considered as the upland fraction. As simulated liquid soil moisture in the top soil

1594   layer responds to changes in environmental conditions the dynamic wetlands expand and

1595   contract. The upper and lower soil wetness thresholds are summarized in Table A1 and

1596   adapted to yield realistic geographical and latitudinal distribution of wetland extent compared

1597   to observation-based estimates.

1598

1599

1600

Grid cell fraction with slope < 0.2% which can potentially become a wetland, climate permitting

a) 0.5° degree resolution

b) 2.81° degree resolution

0.00   0.20   0.40   0.60   0.80   1.00
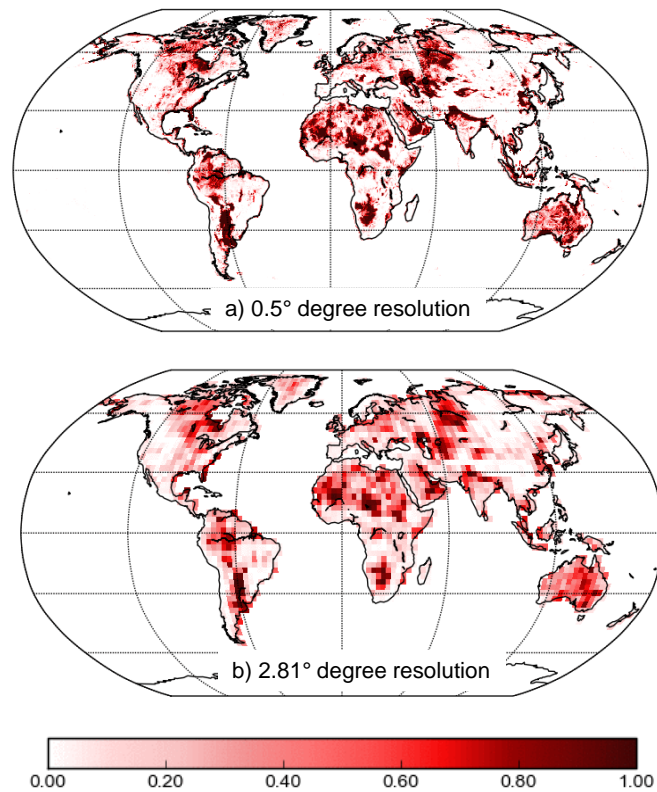
1601

Figure A1: Fraction of grid cell with slopes less than the threshold of 0.002 (i.e. 0.2% slope) at a) 0.5° and b) 2.81° spatial resolutions, respectively.

1604

Table A1: The upper and lower soil wetness thresholds for three latitudinal bands used in equation (1) to determine fractional wetland coverage in a given grid cell.

1607
1608

	Latitudinal band		
	40°N to 90°N	35°S to 40°N	90°S to 35°S
w_{low}	0.45	0.55	0.70
w_{high}	0.90	0.99	0.99

1609
1610

1611

1612 **Appendix B: Driving data**

1613

1614
1615
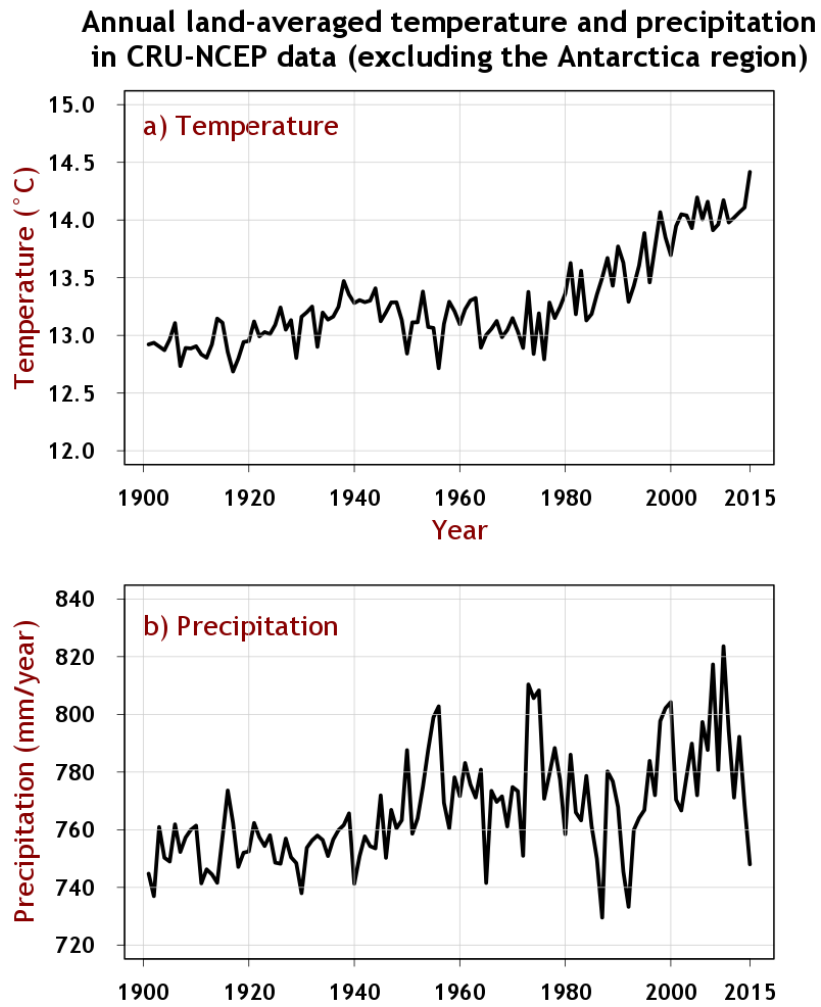
1616

1617 Figure B1: Annual land-averaged temperature and precipitation in version 7 of the CRU-
1618 NCEP data for the period 1901-2015, excluding the Antarctica region, that are used to drive
1619 the CLASS-CTEM model.

1620

1621

1622

1623

1624

1625

Globally-averaged CO$_2$ and CH$_4$ concentrations used to drive the CLASS-CTEM model
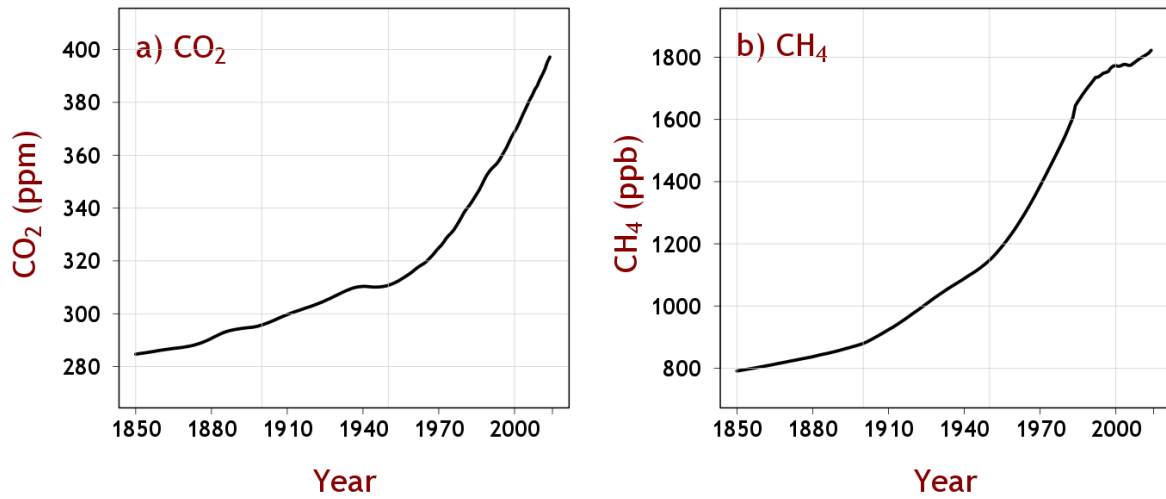
1626

Figure B2: Globally-averaged CO$_2$ and CH$_4$ concentrations used to drive the CLASS-CTEM model.

1629

1630

1631

1632 Appendix C: Selected model results used to interpret methane emissions from wetland and
1633 fire.

1634

1635
1636
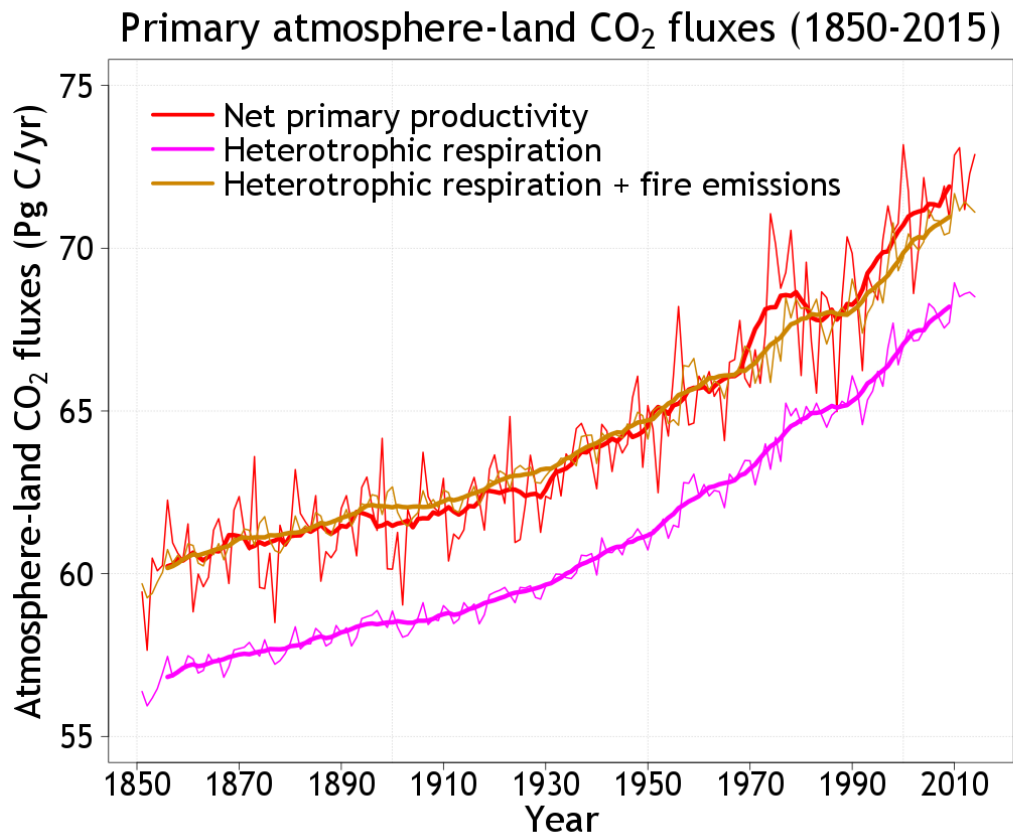
1637
1638
1639 Figure C1: Time evolution of simulated net primary productivity (NPP) and heterotrophic
1640 respiration in the historical simulation both of which increase in response to increase in
1641 atmospheric CO_2 concentration. The thin lines show annual values while the thick lines
1642 represent their 10-year moving average. When fire CO_2 emissions are added to heterotrophic
1643 respiration the total amount is equal to NPP especially during 1850s as the case should be
1644 when the system is in equilibrium and net atmosphere-land CO_2 flux (equal to NPP –
1645 heterotrophic respiration – fire emissions) is near zero. Later in the 20th century and early 21st
1646 century, NPP is greater than the sum of heterotrophic respiration and fire CO_2 emissions,
1647 which creates the sink over land that is currently observed.
1648

1649

1650

1651

1652

Global area burned (million hectares, Mha)
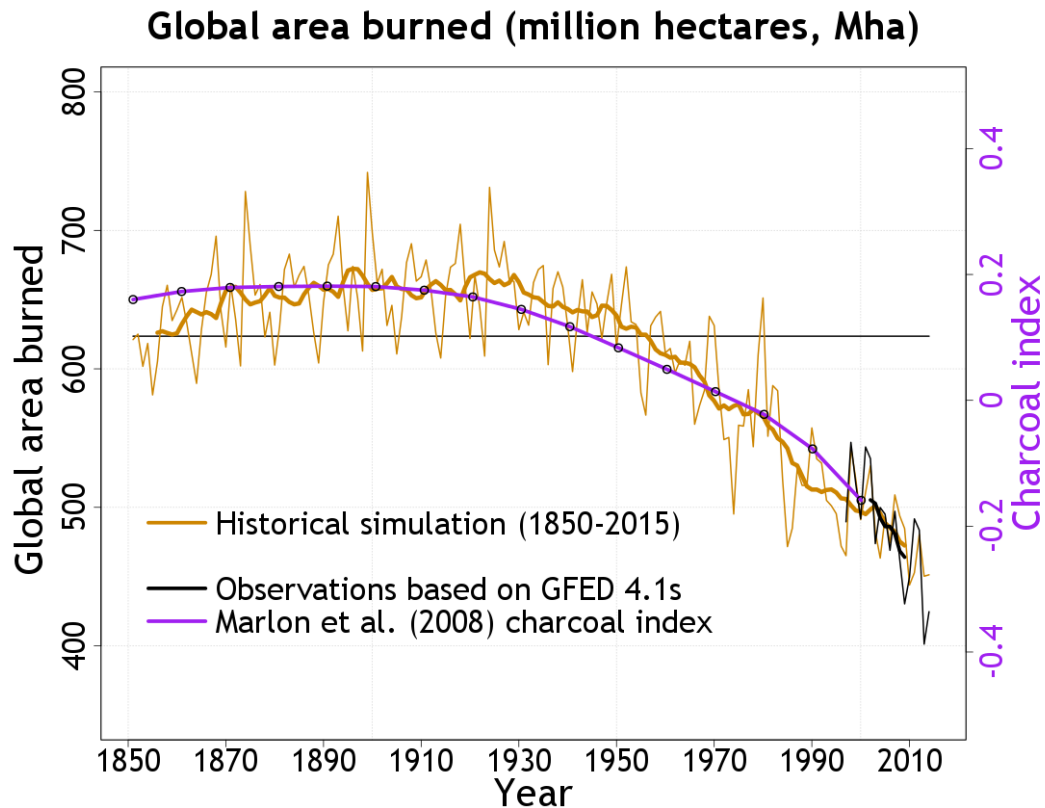
1653

Figure C2: Comparison of global area burned from the transient 1851-2015 historical
simulation (dark yellow line). The thick dark yellow line is the 10-year moving average.
Observation-based area burned (black line) are based on the GFED 4.1s data set. Model
results are also compared to decadal charcoal index from version 3 of the Global Charcoal
Database (purple line). Charcoal index is a proxy for burning and not for area burned per se
and therefore only provides a qualitative measure.

1660